Mechanical response of dot-by-dot wire-and-arc additively manufactured 304L stainless steel bars under tensile loading

Published Version:
Mechanical response of dot-by-dot wire-and-arc additively manufactured 304L stainless steel bars under tensile loading / Laghi V.; Palermo M.; Tonelli L.; Gasparini G.; Girelli V.A.; Ceschini L.; Trombetti T.. - In: CONSTRUCTION AND BUILDING MATERIALS. - ISSN 0950-0618. - STAMPA. - 318:(2022), pp. 125925.1-125925.19. [10.1016/j.conbuildmat.2021.125925]

Availability:
This version is available at: https://hdl.handle.net/11585/841748 since: 2024-03-07

Published:
DOI: http://doi.org/10.1016/j.conbuildmat.2021.125925

Vittoria Laghi, Michele Palermo, Lavinia Tonelli, Giada Gasparini,
Valentina Alena Girelli, Lorella Ceschini, Tomaso Trombetti

Mechanical response of dot-by-dot wire-and-arc additively manufactured 304L stainless steel bars under tensile loading

In: Construction and Building Materials, Volume 318, 2022

The final published version is available online at:

https://doi.org/10.1016/j.conbuildmat.2021.125925

Mechanical response of dot-by-dot Wire-and-Arc Additively Manufactured 304L stainless steel bars under tensile loading

Vittoria Laghi Ph.D[1]*, Michele Palermo Ph.D[1], Lavinia Tonelli Ph.D[2], Giada Gasparini Ph.D[1],
Valentina Alena Girelli Ph.D, Lorella Ceschini Ph.D[2], Tomaso Trombetti Ph.D[1]
*corresponding author: vittoria.laghi2@unibo.it, ORCiD ID: https://orcid.org/0000-0001-8395-2194
[1]Department of Civil, Chemical, Environmental and Materials Engineering (DICAM) - University of Bologna, Viale del Risorgimento, 2 – 40136 Bologna, Italy
[2]Department of Industrial Engineering (DIN) - University of Bologna, Bologna (Italy)

Abstract

With the advent of a new arc-based additive manufacturing (AM) process, referred to as Wire-and-Arc Additive Manufacturing (WAAM), the scale of the metal printed parts increased up to several meters, thus becoming suitable for large-scale applications in marine, aerospace and construction sectors. However, specific considerations in terms of geometrical and mechanical properties ought to be made in order to effectively use the printed outcomes for structural engineering purposes. The introduction of the novel printing strategy referred to as "dot-by-dot", consisting in successive drops of molten metal, enabled the use of WAAM for complex lattice structures, made by continuous grids of WAAM bars. Nevertheless, their proper design requires an accurate evaluation of the influence of the non-negligible inherent geometrical irregularities on the mechanical response of the bars. Hence, extensive experimental work is needed in order to evaluate the mechanical response of WAAM bars with geometrical imperfections.

The present study is thus focused on the assessment of the mechanical response in tension of WAAM-produced 304L stainless steel small bars in terms of key effective mechanical parameters. As such, the mechanical characterization through tensile tests is supported by microstructural investigations and detailed studies on the geometrical features. Three batches of bars are studied, each one printed at different build angles representative of limit cases for practical applications. The microstructural analysis confirms the preferential grain orientation typical of WAAM process for all three build angles. The results of the geometrical and mechanical characterization clearly evidence the non-negligible influence of the inherent geometrical imperfections on the mechanical response in tension of the printed bars, with a detrimental effect of the build angle on the main key effective mechanical parameters. Overall, the results highlight the need of specific investigations on both geometrical and mechanical properties of WAAM bars for structural design purposes.

Key words

Additive Manufacturing; Wire-and-arc; Stainless steel; Mechanical response; Tensile tests; Microstructural analysis.

1. Introduction

Among different metal-based Additive Manufacturing (AM) processes, Wire-and-Arc Additive Manufacturing (WAAM) results to be the most suitable for construction applications to realize large structural components and real-scale structural elements with ideally no geometrical limitations in shape and size, while still maintaining good mechanical performances [1–3]. In the last few years, various research studies focused on the microstructural and mechanical features of different WAAM processed metals, such as steels [4-16], titanium [17–19] and aluminum alloys [20–23]. Regarding WAAM of steels, recent studies investigated their mechanical response with specific reference to the inherent issues proper of the printing process, i.e. the anisotropic nature of the printed parts [5–8,14,16,24] and the geometrical irregularities which might affect their mechanical behavior [25,26]. The first explorations of WAAM applications in construction were conducted with the layer-by-layer deposition strategy, to realize planar (shell) elements by deposition of successive layers of molten metal, see e.g. [27–29]. More recently, an alternative single-cycle deposition strategy (also referred to as skeleton WAAM [30] and hereafter as “dot-by-dot” deposition) was investigated to realize bars and lattice elements [31] through the deposition of successive drops of molten metal. Current research is also investigating the application of the printed bars as steel reinforcement for innovative 3D-printed concrete structures [32,33]. Nonetheless, given the novelty of the printing strategy, the reported research activity on this technique is still very limited [34–36].

WAAM-produced elements are generally characterized by specific features related to the printing process which should be properly investigated: (i) different material properties with respect to the conventional wrought counterpart; (ii) possible anisotropic mechanical behavior with respect to the printing direction; (iii) geometrical irregularities related to the WAAM deposition strategy (either layer-by-layer or dot-by-dot). Therefore, it becomes crucial to study WAAM-produced parts from the microstructural, geometrical and mechanical point of view in order to assess their mechanical response for structural design purposes.

Over the last years, the authors have been studying the microstructural and mechanical features of WAAM-produced ferrous and non-ferrous metals (304L austenitic stainless steel and 5083 aluminum alloy) [25,37–42]. With specific focus on the austenitic stainless steel, the results revealed a marked orthotropic nature, related to the strongly oriented microstructure [40]. The mechanical characterization highlighted appreciable differences in the tensile response of specimens oriented at different directions with regard to the printing layers [38]. Moreover, specific studies were carried out to evaluate the influence of the geometrical irregularities and surface roughness on the mechanical response of as-built WAAM plates [25].

As for the layer-by-layer printed plates, also dot-by-dot printed bars need to be studied in terms of mechanical response accounting for their inherent geometrical irregularities. Indeed, a typical WAAM bar has one main building direction and a nominal constant cross-section (corresponding to the weld drop). Hence, for structural design purposes, it can be ideally assumed as a straight cylindrical element having circular cross-section with constant along-the-length area, even though the actual printed outcome is characterized by non-negligible lack of straightness and cross-section variation, due to the spot-like deposition. Concerning the mechanical behavior, given the bar geometry and the relatively small cross-section (usually of the order of 5 to 6 mm diameter) of the specimens to be tested, machining process becomes quite challenging and costly for practical applications. Hence, specific considerations on both geometrical and mechanical features of as-built printed bars should be addressed.

Another important aspect specific of the dot-by-dot printing process is the relative inclination of the torch and the nozzle. In this regard, very recently, Silvestru et al. [35] performed an investigation on WAAM-produced mild steel bars printed at different inclinations of the build angles (e.g. the inclination of the printed bar with respect to the vertical gravity axis) and nozzle angles (e.g. the inclination of the nozzle with respect to the printed bar) by means of 3D laser scanning, tensile tests and non-linear finite element analysis. The results of the study indicated that both the built angle and the nozzle angle have a detrimental effect on the geometrical irregularities (variation along the length of the cross-sectional area), while they did not provide a significant effect on the mechanical properties as evaluated on machined specimens. On the other hand, the as-built bars evidenced non-negligible reduction on strength, elongation and ductility.

This study aims at providing the first results on an extensive work devoted to assess the mechanical response of WAAM stainless steel bars for structural design purposes. In particular, the study here presented is focused on the mechanical response in tension of single bars printed at three different build angles. The results are aimed at evaluating the influence of both build angle and geometrical irregularities (proper of the selected printing process) on the mechanical properties. For this purpose, detailed geometrical characterization is carried out on two levels: (i) a specimen-to-specimen characterization to assess the variability of the geometry within the same batch, and (ii) an inherent characterization on the single bar to assess the variability of the geometry along the element. Additional microstructural investigations are also provided through conventional metallographic analyses, based on the use of optical and scanning electron microscopy. The mechanical response is then estimated through tensile tests on as-built bars to assess the key effective mechanical parameters of WAAM bars useful for structural design purposes.

The paper is organized as follows. Section 2 provides the problem formulation by introducing the key aspects influencing the mechanical response of a bar with imperfections through a simple mechanical model. The aim is to highlight, from a qualitative point of view, the potentially major influence of both geometrical irregularities and material constitutive behavior on the global force-elongation response of steel bars with imperfections. Section 3 illustrates the aim and the methods adopted to carry out the experimental tests, whose results are reported in Section 4. Section 5 provides an interpretation of the mechanical response of WAAM bars based on the experimental results. Some concluding remarks and recommendations are finally drawn.

2. Problem formulation of the mechanical response of a steel bar with geometrical imperfections

2.1 General case of a steel bar with geometrical imperfections

Generally speaking, the mechanical behavior of a steel bar can be severely affected by the presence of geometrical imperfections (e.g. cross-sectional variations along the longitudinal axis), especially when considering ultimate deformation capacity. A relevant example is represented by the phenomenon of the pitting corrosion of prestressing strands and rebars that may cause severe reductions of ultimate strength and deformation capacities [43–45] up to catastrophic failure (e.g. Polcevera bridge in Northern Italy [46,47]). In fact, in such case the axial stress field induced by an external axial load is not uniform along the element length and local stress concentrations and early plasticization may occur with the remaining part still in the elastic phase. This leads to premature failure with limited ductility capacity. The influence of local stress concentration and plasticization in the global force-elongation capacity of the single bar strictly depends on the specific type of geometrical imperfections and on the material constitutive model [48].

For a first appraisal of the influence of these aspects on the tensile response of a steel bar with a geometrical defect, an element of length L_0 with an idealized defect is considered. The ideal defect is localized in a portion of length L_c (which can be described by the dimensionless parameter $\lambda=L_c/L_0$) characterized by a reduced cross-sectional area A_c (which can be described by a dimensionless parameter $\rho=A_c/A_0$, where A_0 indicates the cross-sectional area of the defect-free bar). At first approximation, the damaged element can be modelled by two non-linear springs connected in series. The graphs of Figure 1 reproduce the qualitative force-elongation behavior of the whole damaged element as compared to the corresponding undamaged one. The behavior is studied by considering three different constitutive models: an elastic-perfectly plastic (EPP) model, an elasto-plastic with hardening (EPH) model and a non-linear Ramberg-Osgood (RH) [49] model. Two different steel types are also considered: low-strength/high-ductility steel and high-strength/low-ductility steel (μ_m indicates the material ductility).

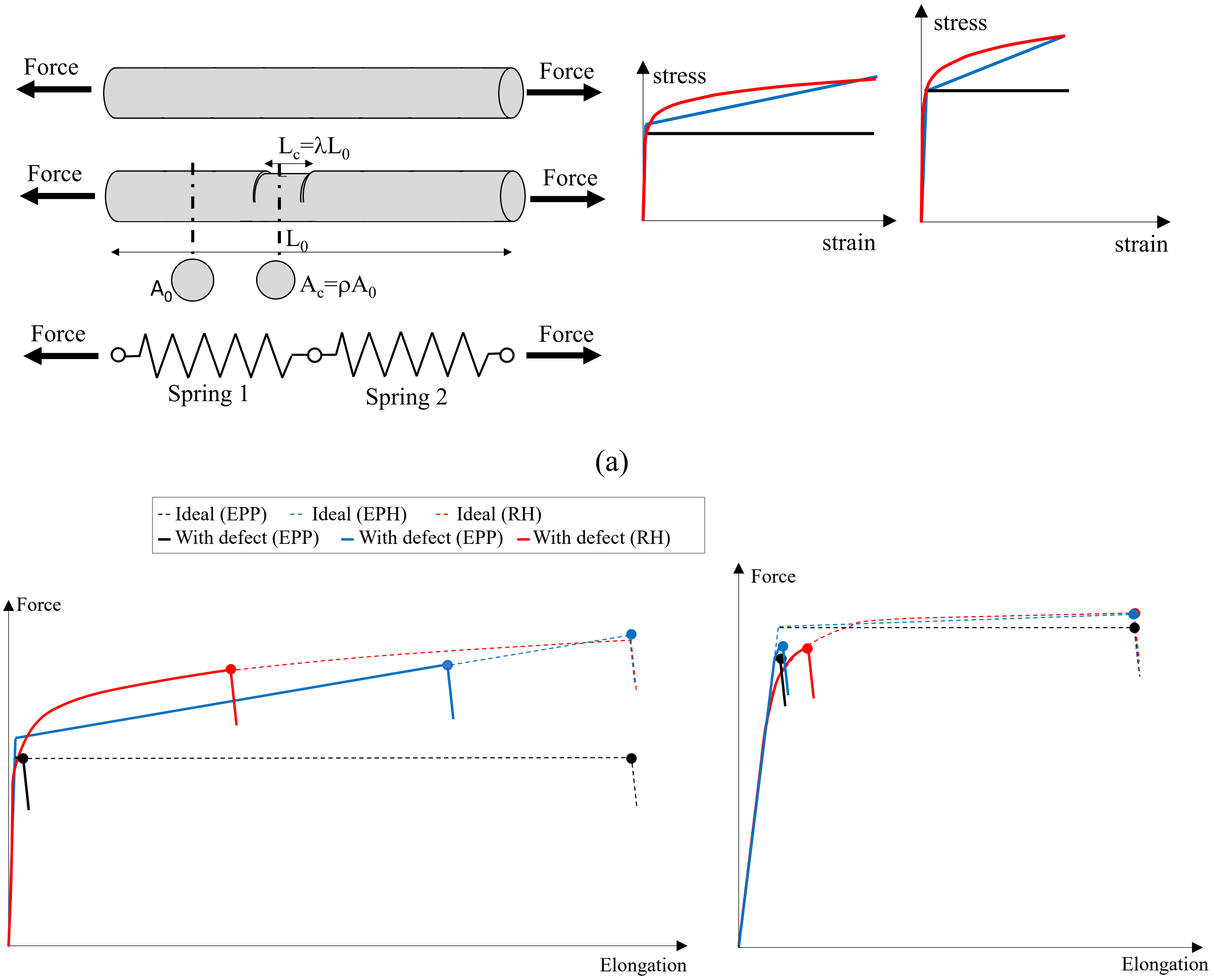

(a)

(b) (c)

Figure 1: (a) Mechanical model of a bar with geometrical imperfections; Force-elongation of a metal bar with a single geometrical defect (characterized by ρ=0.9 and λ=0.01) for (b) high-ductility (μ_m=100) material behavior and (c) low-ductility (μ_m=10) material behavior.

Fig.1 b and c clearly show the very large variability of the force-elongation behavior in tension due to the coupling of geometrical irregularities and non-linear material constitutive behavior. Hence, from a structural design point of view it becomes of high interest to assess the whole element's response when subjected to tensile force with specific focus on the influence of the geometrical irregularities.

For the present study, the WAAM bars are studied at a macro scale through geometrical and mechanical characterization to derive the effective stresses and strains evaluated from the whole force-elongation response.

2.2 Specific case of WAAM bars

Dot-by-dot printed elements are produced through successive deposition of metal droplets along the main axis (z-axis). This results in 3D elements (bars) of constant nominal diameter directly related to the drop of liquid metal, with one main growing direction. Usually, for current printing technologies the nominal diameter of WAAM bars varies within the range of 4 to 8 mm [50]. However, for dot-by-dot printed bars the successive deposition of metal droplets causes a variation of their real diameter along the height of the bar of the order of around 0.5 mm, resulting in a visible surface roughness, similarly to the one generated by the layer-by-layer deposition for continuously-printed plates [25]. Additionally, the deposition process can also induce some lack of straightness due to inaccurate positioning of the torch, which should also be investigated (Figure 2a). Hence, with regards to dot-by-dot WAAM bars, the deposition strategy results in a non-uniform circular cross-section and non-straight longitudinal axis (formed by the polyline connecting the centroids of each circular cross-section).

The nominal geometry of the digital model for the investigated WAAM bars consists in a uniform full cylinder with straight longitudinal axis (coincident with z-axis of the cylindrical coordinate system, Figure 2b). The geometry is described by the nominal bar height (H_n) and the nominal cross-sectional diameter (d_n). The real geometry of a WAAM bar is, instead, more complex and can be described by a solid element with non-uniform circular cross-section varying along its length and a non-straight longitudinal axis (Figure 2c). The coordinate system adopted for the geometrical description has the origin in the centroid of the base cross-section (e.g. $C(z=0)$) and the z-axis corresponding to the one connecting the centroid of the base cross-section and the one of the top cross-section (e.g. $C(z=H)$).

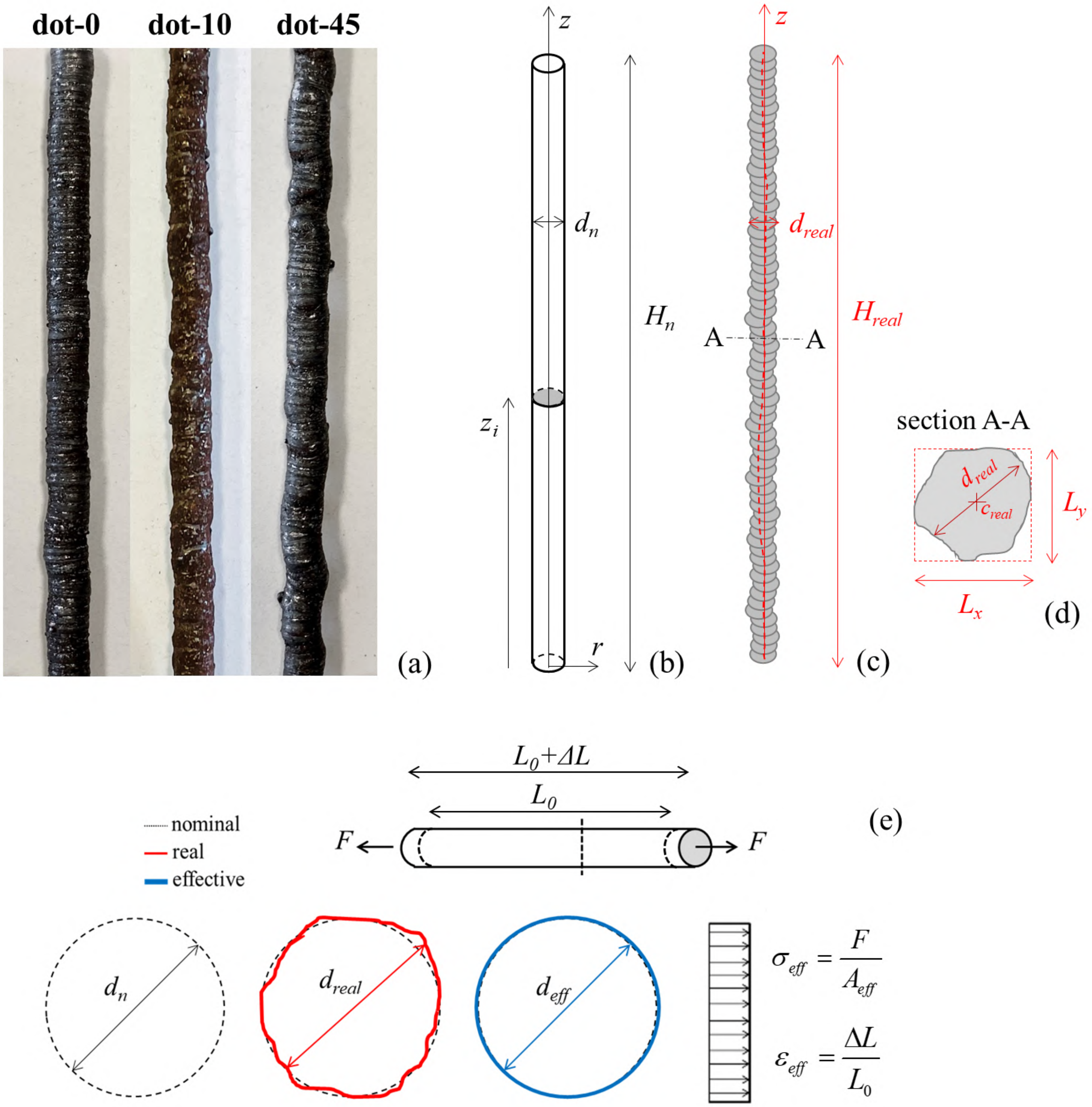
dot-0
dot-10
dot-45
(a)
z
d_n
H_n
z_i
r
(b)
z
d_{real}
H_{real}
A
A
(c)
section A-A
d_{real}
c_{real}
L_y
L_x
(d)
$L_0+\Delta L$
L_0
F
F
(e)
nominal
real
effective
d_n
d_{real}
d_{eff}
$\sigma_{eff} = \frac{F}{A_{eff}}$
$\varepsilon_{eff} = \frac{\Delta L}{L_0}$

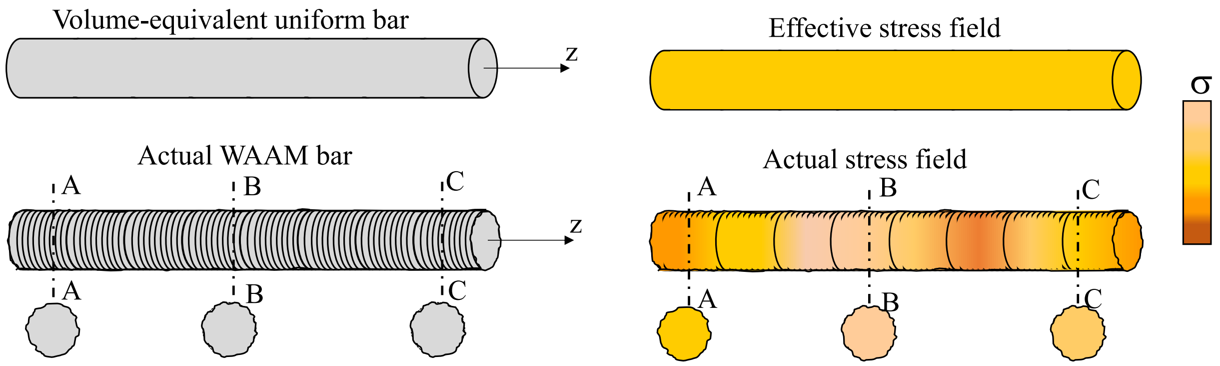
Volume-equivalent uniform bar
z
Effective stress field
σ
Actual WAAM bar
A
B
C
z
A
B
C
Actual stress field
A
B
C
A
B
C

(f)

Figure 2: (a) Close-up view of the geometrical description of WAAM bars (printed at 45° and 0° build angle, respectively; bars printed at 10° build angle resulted similar to those at 0°, hence not included); (b) digital model and (c) corresponding printed element of a WAAM bar and (d) detail of one real cross-section; (e) nominal, real and effective cross-sections of the WAAM bar. (f) effective vs actual (true) stress fields.

As a consequence of these geometrical irregularities, it is clear that a detailed description of the mechanical tensile response of the real WAAM bar would require the evaluation of local true stress and strain values. These values vary along the longitudinal axis due to the variation of the cross-sectional area along the length of the bar ($A=A(z)$) and due to the presence of small eccentricities due to the lack of straightness, possibly inducing also additional bending stresses (Figure 2f). Such detailed evaluation would require ad-hoc measurements during experimental tests (e.g. with the use of optical monitoring systems) and complex digital twins, see e.g. [3,27].

As an alternative, from a structural design point of view, the mechanical response of the entire real WAAM bar could be described in terms of effective mechanical parameters (e.g. effective stresses and strains) which are associated to the effective volume-equivalent cross-sectional area A_{eff} uniform along the whole length of the element as follows:

$$\sigma_{eff} = \frac{F}{A_{eff}} \tag{1}$$

$$\varepsilon_{eff} = \frac{\Delta L}{L_0} \tag{2}$$

Clearly, such effective parameters could be adopted for the design of WAAM bars having the same geometrical properties and realized with the same printing parameters as the ones studied hereafter.

3. Experimental tests on WAAM bars

3.1 The aim and approach

The aim of the experimental work is to assess the mechanical response of WAAM bars for structural design purposes. From the mechanical point of view, the response is studied under different loading conditions: tension, compression and bending. The tests are carried out on as-built bar, considering the real conditions at which they will be subjected for construction applications (i.e. with no post-processing milling treatments). The results of the experimental tests are then interpreted in terms of effective quantities (i.e. effective stresses and strains) accounting for the variability and possible detrimental effects associated to the inherent geometrical irregularities. Detailed microstructural analyses are also carried out to highlight the microstructure features of WAAM dot-by-dot stainless steel, also considering possible defects.

The present study is focused on the results of tensile tests carried out on WAAM bars by estimating: (i) the geometrical irregularities of both the single specimen (inherent variability) and of the entire batch (specimen-to-specimen variability), (ii) the microstructural features proper of the selected printing process, (iii) the effective mechanical parameters for structural design purposes. Table 1 summarizes the specimens' characteristics and tests.

In order to account for the possible influence of the printing direction (with respect to the vertical axis) on the overall mechanical response of the printed bars, three different build angles (b-a) are considered, consisting in the angle between the axis of the WAAM bar (*z*-axis) and the vertical axis (perpendicular to the base platform). The nozzle angle (n-a), consisting in the angle between the axis of the WAAM bar (*z*-axis) and the nozzle axis, was set equal to 0° for all batches. In detail, the specimens were printed with build angles equal to 0° (dot-0), 10° (dot-10) and 45° (dot-45) (Figure 3). The case of 0° and 45° build angles correspond to the common limit conditions (0° and 45°) for practical applications. The case of 10° build angle corresponds, instead, to a commonly adopted value for lattice structural elements (see e.g. [31]).

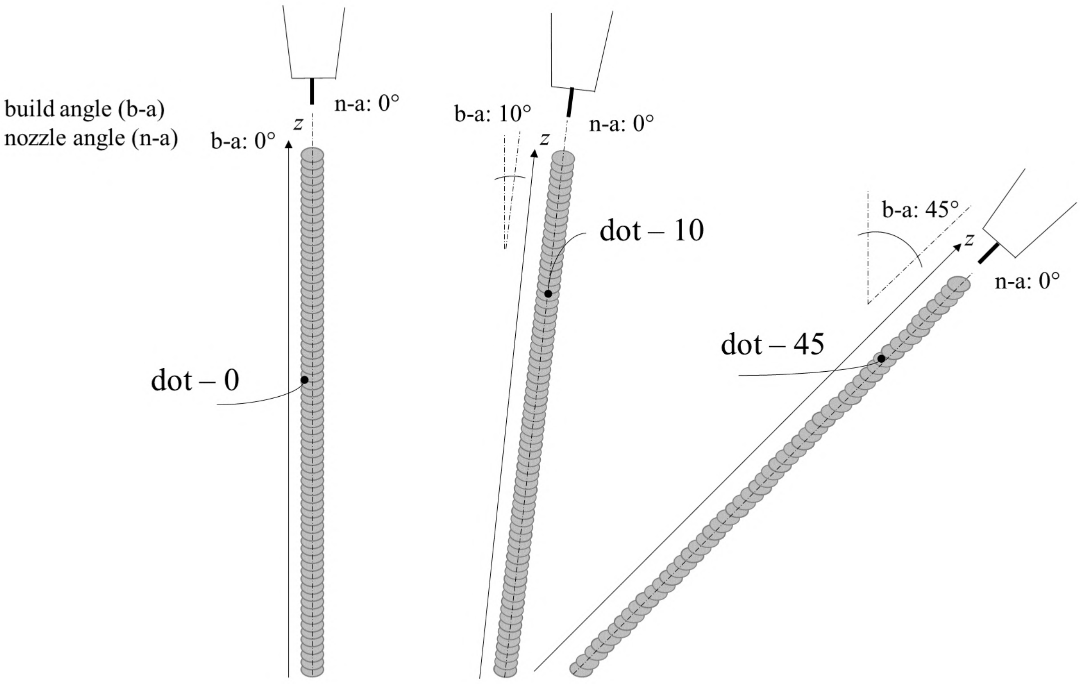

Figure 3: Graphical representation of the WAAM bars printed with three different build angles (b-a):0° (dot-0), 10° (dot-10) and 45° (dot-45).

Table 1: Summary of specimens' characteristics and tests.

Build angle	**Specimen ID**	**Nominal length**	**Nominal diameter**	**Geometrical characterization**	**Mechanical characterization**	**Quantity**
0°	dot-0	H_n=250 mm	d_n=6 mm	Hand Volume 3D scan	Tensile	10
10°	dot-10	H_n=250 mm	d_n=6 mm	Hand Volume	Tensile	10
45°	dot-45	H_n=200 mm	d_n=6 mm	Hand Volume 3D scan	Tensile	9

3.2 Material and process

The WAAM bars studied in the present work were produced by MX3D [51] with Gas Metal Arc Welding (GMAW). A commercially-available ER308LSi stainless steel welding wire (1 mm diameter) grade, supplied by *Oerlikon* [52], was used as feedstock wire. The nominal chemical composition of the wire is reported in Table 2. Welding speed and wire feed rate were 15-30 mm/s and 4-8 m/min, respectively. The employed shield gas was 98% Ar and 2% CO_2 at a flow rate of 10-20 L/min, the current and arc voltage of the deposition process were 100-140 A and 18-21 V respectively, while the deposition rate was 0.5-2 kg/h. Values of the process parameters are provided within typical ranges adopted by MX3D. For further information the interested reader could refer directly to MX3D. The substrate was a printing plate of 1000 x 1000 x 30 mm, with welded H-type beams as support.

3.3 Chemical and microstructural characterization

The chemical composition of WAAM bars was verified by Glow Discharge Optical Emission Spectroscopy (GDOES), with a sputtered burnt spot of 2.5 mm diameter. Microstructural characterization was then carried out in order to relate the mechanical parameters to the microstructural features typical of additively manufactured parts. Samples for microstructural characterization were extracted from dot-0, dot-10 and dot-45 bars. In the analyses, two directions were considered: the longitudinal one (i.e. parallel to the *z*-axis, as defined in Figure 2) and the transverse one (i.e. perpendicular to the *z*-axis). Metallographic sections were embedded in a phenolic resin and polished up to a mirror finish by following standard metallographic preparation techniques [53]. Chemical etching with 20 s immersion at ambient temperature in Vilella's reagent (1 g picric acid, 5 mL hydrochloric acid and 100 mL ethanol [54]) was adopted to reveal general microstructural features. The presence of ferrite was then confirmed using a specific color etching, described in [55]. Etched metallographic sections were observed by means of optical and field emission gun scanning electron microscopy (FEG-SEM). An energy-dispersive spectroscopy (EDS) system, available inside the FEG-SEM microscope, was employed for semi-quantitative compositional microanalyses. In addition, to further investigate fracture path and failure mechanisms, also samples extracted along the longitudinal axis of bars, in a region close to the fracture surface, were subjected to the same metallographic preparation described above and then observed with an optical microscope.

3.4 Geometrical characterization

Given the non-uniform cross-section and not-perfectly-straight longitudinal axis, the geometrical characterization consisted in: (i) evaluating the real cross-sectional area along the longitudinal axis; (ii) identifying the shape of each cross-section (if it can be assumed as circular at first approximation); (iii) identifying the real longitudinal axis (corresponding to the polyline connecting the real cross-sectional centroids); (iv) evaluating the volume-equivalent cross-section (for the evaluation of the effective stresses).

First, the specimen-to-specimen geometrical variability was assessed for all specimens then tested under tensile loading condition. For each of them, the estimation of the volume-equivalent, or effective, cross-sectional area (A_{eff}) of each specimen was taken by means of volume measurements, based on the Archimedes' principle, as also adopted in [25,26]. From them, the effective diameter is computed as $d_{eff} = \sqrt{\frac{4A_{eff}}{\pi}}$ (Figure 2e). The measures were taken for each entire specimen before testing. This procedure was previously applied for as-built specimens taken from WAAM-produced plates, as also presented in [25,26].

Then the local geometrical measurements were performed through 3D scanning technique considering two WAAM bars (printed at 0° and 45° build angles). From the 3D model, a total of 120 cross-sections (equally spaced at 2 mm) along the length of each specimen were extracted, from which information regarding the cross-sectional diameter and centroid was analyzed. A structured-light projection Artec Spider 3D scanner [56] was used for the 3D scan acquisition. The 3D model of the scanned bar consisted of around 40 million triangular elements, with a medium-points spacing of about 0.10 mm.

In detail, for each considered cross-section (located at height z) of the real WAAM bar, the cross-sectional area $A_{real}= A_{real}(z)$ and the corresponding centroid $C_{real}=C_{real}(z)$ were measured. In addition, from the cross-sectional area A_{real} an equivalent cross-sectional diameter was identified as follows: $d_{real} = \sqrt{\frac{4A_{real}}{\pi}}$. The equivalent real diameter d_{real} was computed considering that the shape of the cross-section is close to that of a circle. This assumption is in line with the digital input model used for the printed bars (see Section 2.2). The discrepancies from the circular shape were computed comparing the values of the two sides of the circumscribed rectangle (L_x, L_y) with the equivalent diameter d_{real} (see Figure 2c). Then, the identification of the real longitudinal axis was performed by connecting the centroids C_{real} (corresponding to the center of mass of each cross-section) of all sections.

3.5 Mechanical characterization

The tensile tests were performed on a universal testing machine of 500 kN load capacity at the Structural Engineering labs of University of Bologna.

The tensile specimens were tested under displacement control with a velocity corresponding to a stress rate of 2 MPa/s according to [57]. A linear deformometer (50 mm gauge length) was adopted to detect the effective strain of the specimens up to yielding (Figure 4).

(a) (b)

Figure 4: (a) Tensile test set-up; (b) typical tensile failure for a dot-0 specimen.

The tensile tests were performed on a total of 29 specimens (10 at 0° build angle, 10 at 10° build angle and 9 at 45° build angle). Elastic Modulus (*E*), 0.2% proof stress ($Rp_{0.2}$), ultimate tensile strength (*UTS*), elongation to failure ($A_{\%}$) and element's ductility (μ_e) were evaluated from the effective stress-strain curves. After the tensile tests, fracture surfaces were analyzed at low magnification by means of a 3D digital microscope and by FEG-SEM, coupled with EDS, for a high magnification investigation.

Vickers hardness measurements (HV$_1$) with a 1 kg load and 15 s dwell time were performed on polished sections extracted from the WAAM bars along the direction parallel and perpendicular to the *z*-axis.

4. Main experimental results

4.1 Compositional analysis

Chemical composition evaluated by GDOES on the printed bars is reported in Table 2 and compared to the nominal composition of the feedstock wire. As the 308L Si wire is commonly adopted for the conventional welding of the AISI 304L (UNS-S-30403) austenitic stainless steel, results were also compared to the reference composition of the latter. Apart from a small difference in the Cr content, the chemical composition of the printed bars fulfilled the specifications for the AISI 304L. An analogous outcome was also found for the case of WAAM plates printed with the same wire [38]. Therefore, as the final goal of WAAM is the fabrication of large structural parts, mechanical properties of WAAM bars are hereafter compared to the requirements reported for the AISI 304L in the European Building Code [58] for the design of steel structures.

Table 2: Chemical composition (wt.%) measured on the WAAM bars compared to the nominal chemical compositions of the wire (given by the supplier, and the 304L (UNS-S-30403) austenitic stainless steels [59]

	C	***Cr***	***Ni***	***Mn***	***Si***	***Co***	***V***	***Mo***	***Cu***	***P***	***S***	***Fe***
Feedstock Wire	0.02	20.00	10.00	1.80	0.85	-	-	0.2	-	<0.025	<0.020	Bal.
WAAM bars	0.01	20.17	9.59	1.23	0.94	-	0.11	0.05	0.03	0.043	0.022	Bal.
AISI 304L	<0.03	18.0-20.0	8.0-12.0	<2.0	<1.0	-	-	-	-	<0.045	<0.03	Bal.

According to the Schaeffler diagram [60] and based on the Cr_{eq} and Ni_{eq} obtained from the chemical composition of bars, both γ-austenite and δ-ferrite (approx. 15 vol.%) phases were expected (Figure 5).

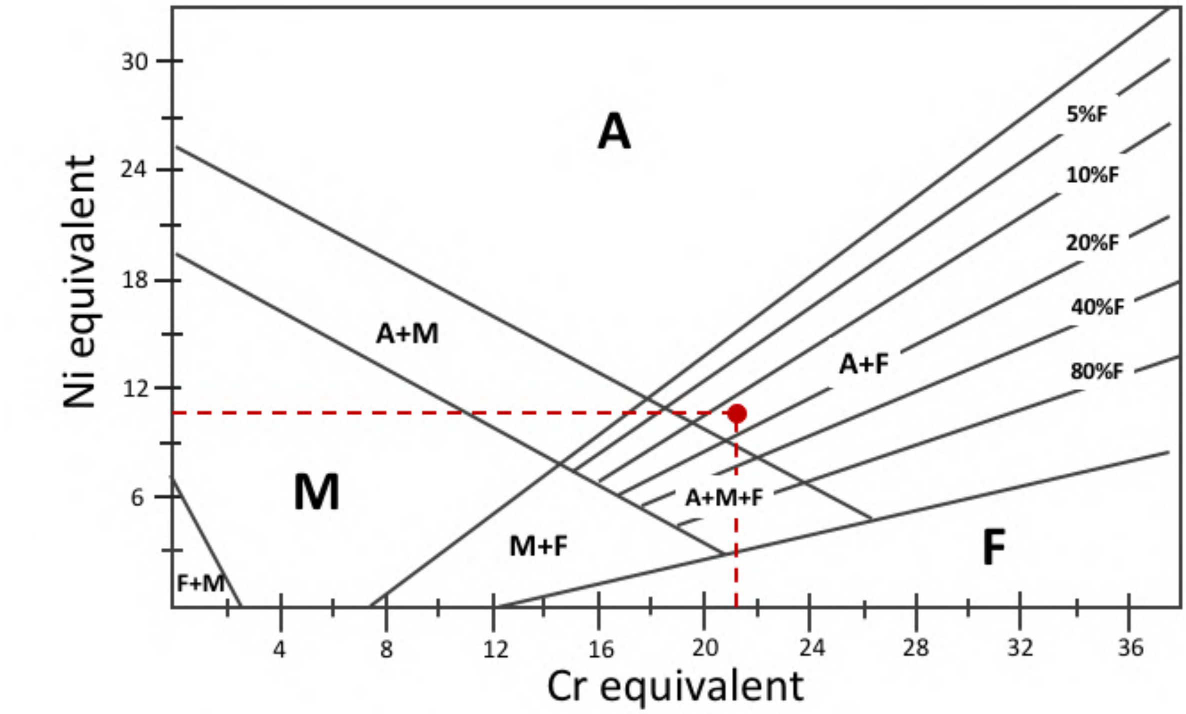

Figure 5: Schaeffler Diagram (adapted from [60]*): in the diagram, red dashed lines outline the* Cr_{eq} *and* Ni_{eq} *values obtained from the chemical composition evaluated on WAAM bars leading to the Austenite + Ferrite (A+F) region*

4.2 Microstructural characterization

As mentioned before, the dot-by-dot methodology involves the subsequent deposition of single metal droplets that rapidly solidify on the previously deposited material, thus forming the layered microstructure typical of additive manufacturing. Low magnification metallographic analyses (Figure 6) give a general view of the microstructure of WAAM bars, in which evidence of the droplet deposition can be found. In particular, by comparing the representative longitudinal sections taken along the *z*-axis of dot-0, dot-10 and dot-45 bars (Figures 6a,b and c), layers formed by the subsequent depositions, whose boundaries are underlined in yellow in the figure, can be seen. In case of dot-0 and dot-10 (Figures 6a,b), layer boundaries are almost perpendicular to the building direction while a slight inclination can be observed for dot-45 bars (Figure 6c). The analyses also evidenced the variability in the bar diameter that will be further addressed in the following section. It is well-documented in the literature that additive processes, like WAAM, often lead to epitaxial grain growth [61]. Due to epitaxy, during the solidification of molten droplets grains grow directly from the previously deposited layer, replicating the same crystallographic orientation and following the maximum thermal gradient. Therefore, the formation of highly-oriented large columnar grains crossing-over layers is promoted. Evidence of this is given in Figures 6d,e,f, where the observation of metallographic sections under polarized light allows to outline epitaxial columnar grains. In the figures, the focus is given to the interlayer region of bars, showing large grains (white dashed lines) that cross-over the layer boundary (yellow dashed lines) without changing their crystallographic orientation. For all the three investigated build angles (0°, 10° and 45°), epitaxial grains followed the direction of longitudinal axis of bars (*z*-axis). In fact, a similar grain orientation was observed for dot-0, dot-10 and dot-45 bars, thus showing no remarkable influence from the different build angles, even if the layer boundaries were almost perpendicular to the *z*-axis in case of dot-0 and dot-10 bars and approximately 45° oriented in case of dot-45 bars.

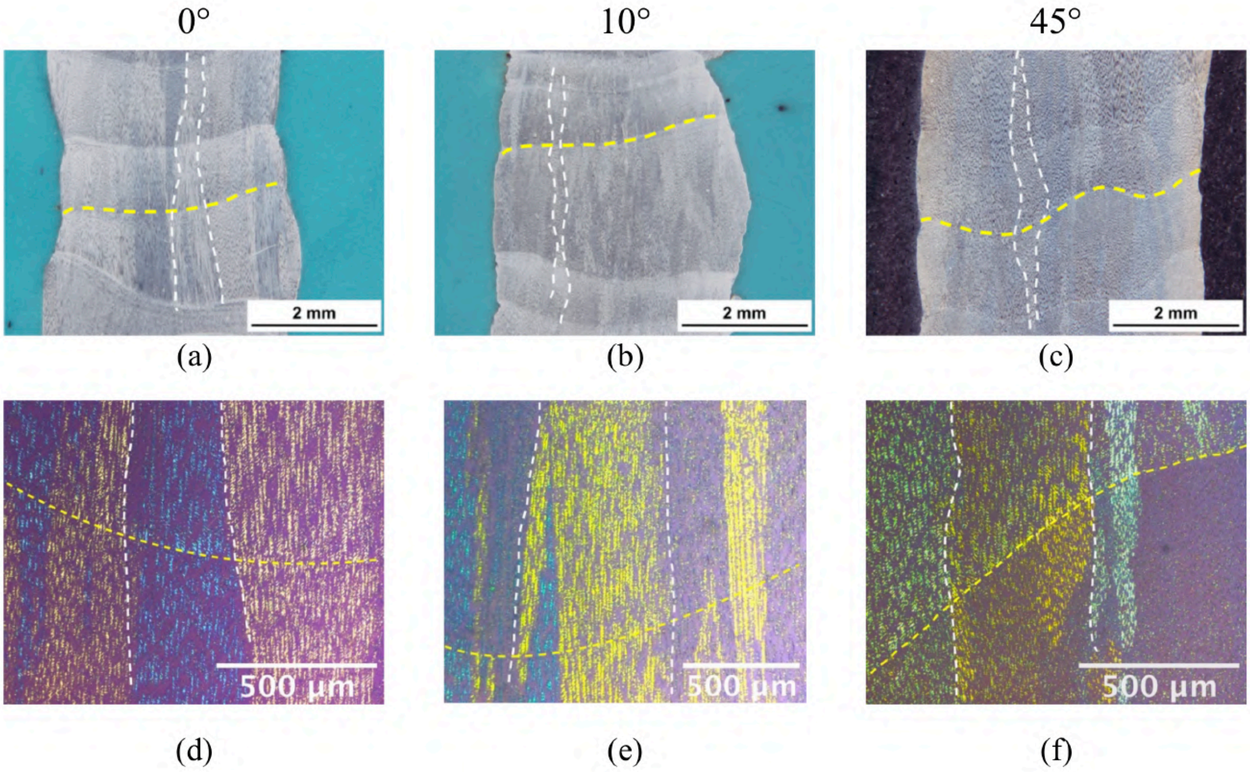

(a) (b) (c)

(d) (e) (f)

Figure 6: Representative low magnification microstructural images taken along the longitudinal axis (z-axis) of the WAAM bars: a, b), c) 3D optical microscopy showing the overall microstructure, d), e), f) color microscopy showing epitaxial growth of columnar grains crossing-over layers. Yellow and white dashed lines underline layer boundaries and epitaxial grains, respectively.

Detail of the solidification structure formed within the large epitaxial grains is given in Figure 7, that compares representative longitudinal and transversal metallographic sections. A fine columnar-dendritic structure can be found inside the long epitaxial grains, for all the investigated build angles. By focusing on the longitudinal sections (Figure 7a,b), it is possible to observe that the columnar dendritic structure is still oriented along the z-axis, thus following the same direction as the epitaxial grains. Similar outcomes were already discussed in a previous paper focusing on WAAM plates [38]. As a consequence of the highly oriented microstructure observed along the longitudinal direction, in the transverse one a homogeneous dendritic structure, with no evidence of preferred orientation, can be resolved (Figures 7c,d).

Two main phases were detected and, based on previous analyses on WAAM plates [38,42] and on the chemical composition of bars (Table 2 and Figure 5), they were identified as: γ-austenite and minor δ-ferrite, the latter located in the interdendritic regions of γ-austenite. According to the ternary Fe-Cr-Ni phase diagram, in fact, a type ferrite-austenite (FA) solidification is expected. In this view, a specific colour etching [55] was used to reveal the presence of δ-ferrite in the austenite matrix (Figure 7b,d). The analysis confirmed the presence of vermicular δ-ferrite (white phase in Figure 7b,d) in the interdentric regions of the γ-austenite, being the predominant phase. The microstructure of all the investigated samples was also analyzed at high magnification by FEG-SEM (Figure 8). FEG-SEM observations confirmed the presence of vermicular δ-ferrite inside the γ-austenite. Phases are highly oriented, in the longitudinal section (Figure 8a), along the z-axis. The δ-ferrite phase was also observed in the transverse sections (Figure 8b), showing, as already discussed, a non-preferred orientation. High magnification analyses also disclosed globular micrometer-sized particles, whose EDS semi-quantitative analyses revealed the presence of O, Mn, S and Si (Figure 8c). Globular nonmetallic phases in titanium-free cast austenitic stainless steels are reported in the literature, present as complex oxygen compounds [62] whose size decrease with increasing cooling rate [63]. Even if in the WAAM process the molten area is shielded with a flux of inert gas, it is possible that minor oxidation phenomena still occur, as recently demonstrated in case of highly reactive materials as Al and Ti alloys [64,65]. The same particles were also observed on the fracture surface of all samples, as discussed in the following Section 3.5. High magnification analyses also revealed a spread spherical micro-porosity in the samples that can be related to both gas occlusion occurring during the WAAM process and, to some extent, to the metallographic preparation that promoted the detachment of the aforementioned non-metallic inclusions from the matrix.

It should be also noticed that in correspondence of the layer boundaries, a discontinuity in the columnar-dendritic structure exists. In fact, due to the complex thermal cycles involved in the deposition of each layer (or droplet), coarsening of the underneath solidified material occurs. By focusing on the micrographs in Figure 6a that shows an interlayer region, it can be seen that in the region immediately above the layer boundary (yellow dashed line) a finer structure can be observed, while in the region below the boundary the structure is coarser. This outcome was observed in correspondence of each layer boundary, regardless the different build angle. Furthermore, analogous results, in case of WAAM plates, was also discussed in the literature [4,66] and in a previous work [42].

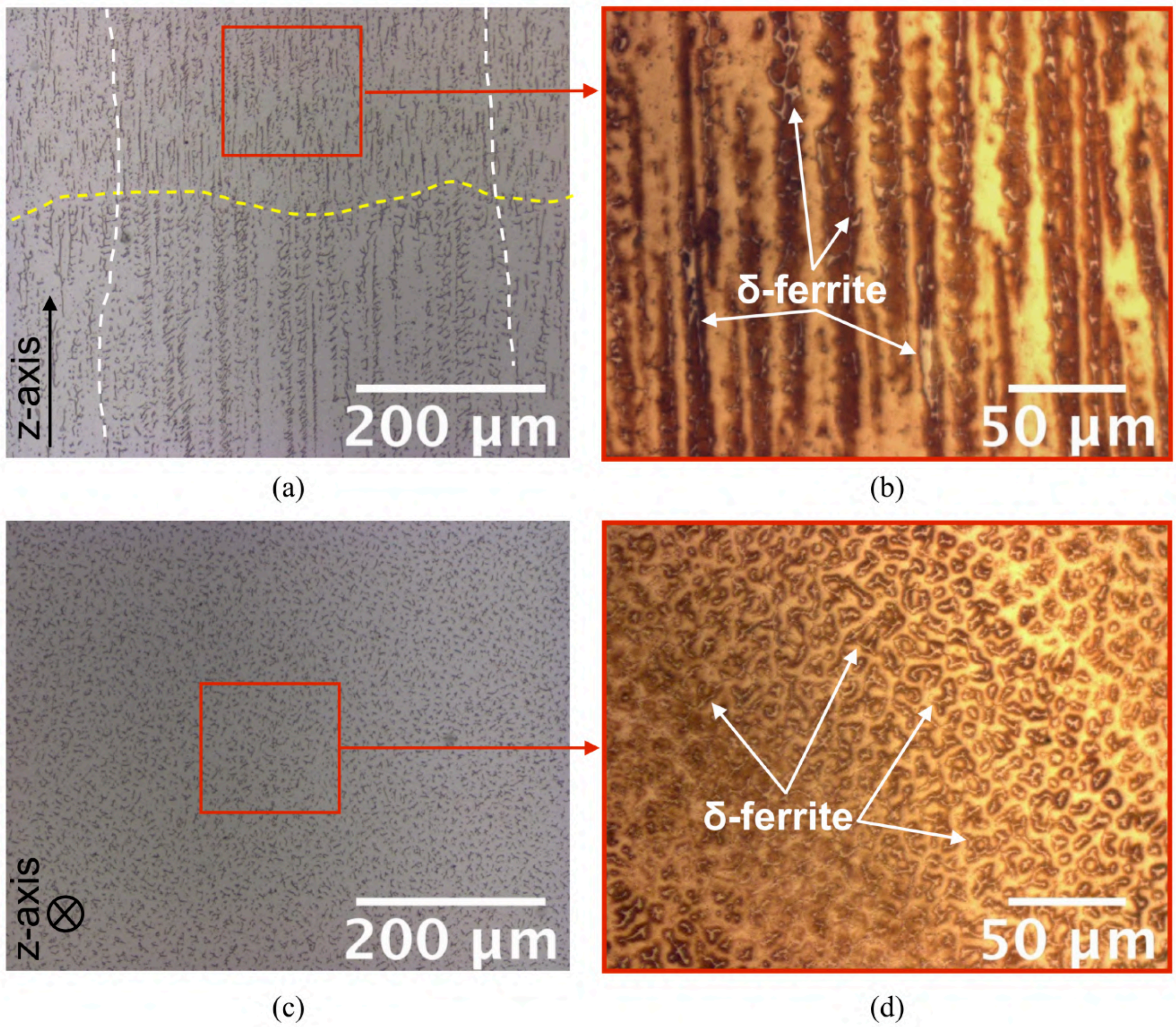

(a) (b)

(c) (d)

Figure 7: Representative optical micrographs of the WAAM bar: a), b) longitudinal sections; c), d) transverse sections. In a) and c) the darker phase is δ-ferrite while the lighter one is the γ-austenite. A specific color etching was applied in b) and d) to reveal the δ-ferrite as the white phase. Yellow and white dashed lines underline layer boundaries and epitaxial grains, respectively.

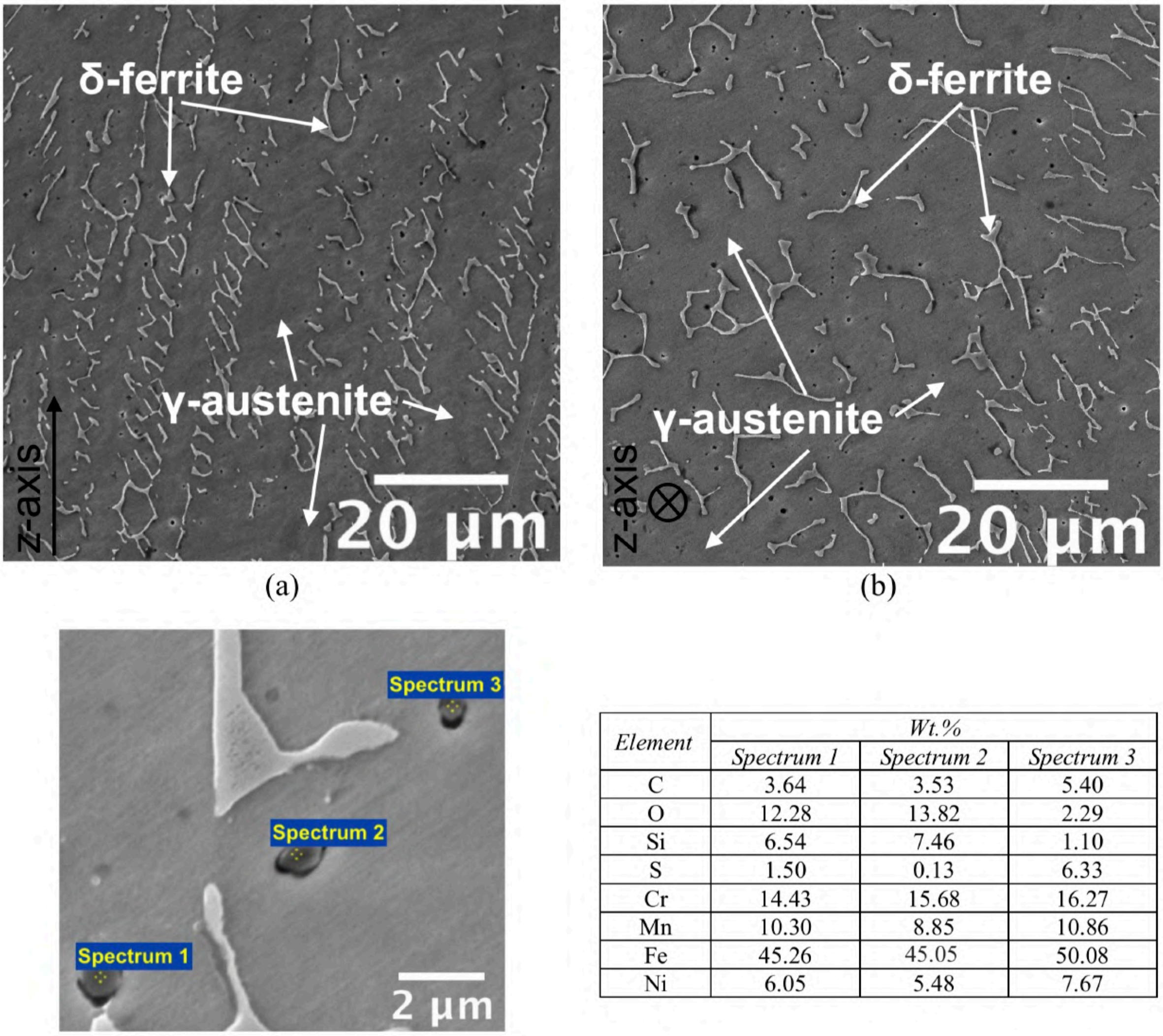

(a)

(b)

Element	*Wt.%*		
	Spectrum 1	*Spectrum 2*	*Spectrum 3*
C	3.64	3.53	5.40
O	12.28	13.82	2.29
Si	6.54	7.46	1.10
S	1.50	0.13	6.33
Cr	14.43	15.68	16.27
Mn	10.30	8.85	10.86
Fe	45.26	45.05	50.08
Ni	6.05	5.48	7.67

(c)

Figure 8: Representative FEG-SEM micrographs of the WAAM bar: a) longitudinal section; b) transverse section; c) EDS analyses performed on inclusions. In the micrographs, the lighter phase is δ-ferrite while the darker one is the γ-austenite, as indicated by arrows.

4.3 Geometrical characterization

4.3.1 Specimen-to-specimen variability

In order to evaluate the effective mechanical properties for structural design purposes, the volume-equivalent cross-section was assumed as the resistant effective cross-sectional area for the calculation of the effective stresses from tensile tests, according to the procedure adopted also in [37,67].

The average effective diameters d_{eff} were equal to (Table 3): 5.92 mm for dot-0 specimens (corresponding to a reduction of less than 5% from the nominal diameter, equal to 6 mm), 5.71 mm for dot-10 specimens (corresponding to a reduction of around 5% from the nominal diameter), and 6.40 mm for dot-45 specimens (corresponding to an increase of around 7% from the nominal diameter). For all of them, the coefficient of variation of the effective diameter was of around 5%. These results are also in line with the measured diameters of WAAM steel bars studied by Silvestru et al. [35], that registered standard deviation values of around 0.20 mm.

Table 3: Mean values and standard deviations of diameters for the bars tested: specimen-to-specimen variability (from volume measures on dot-0, dot-10 and dot-45).

Specimen-to-specimen variability	
Specimen ID	d_{eff} **[mm]**
dot-0	5.92 ± 0.29
dot-10	5.71 ± 0.28
dot-45	6.40 ± 0.29

4.3.2 Inherent variability

From 3D scan acquisition, the 3D models of three bars (one dot-0, one dot-10 and one dot-45) were analyzed to quantify the variability of the local geometrical parameters as identified in Section 3.4. First, it was found that the variability registered for the dot-10 specimen resulted very similar to the one observed for the dot-0 specimen. For this reason, in the present paragraph only the results related to two specimens (one dot-0 and one dot-45) are reported and analyzed.

For each specimen, first the distribution of the cross-sectional area was studied with reference of the 120 sections taken from 3D scan. Figure 9 compares the measured values with the nominal cross-sectional area (A_n= 28.3 mm). Overall, the dot-45 specimen presents slightly higher mean value with respect to the nominal one, while dot-0 presents a lower mean value. The dot-45 specimen also evidences higher scatter in the punctual values (values ranging from 23 to 34 mm^2) with respect to the dot-0 one (values ranging from 23 to 30 mm^2).

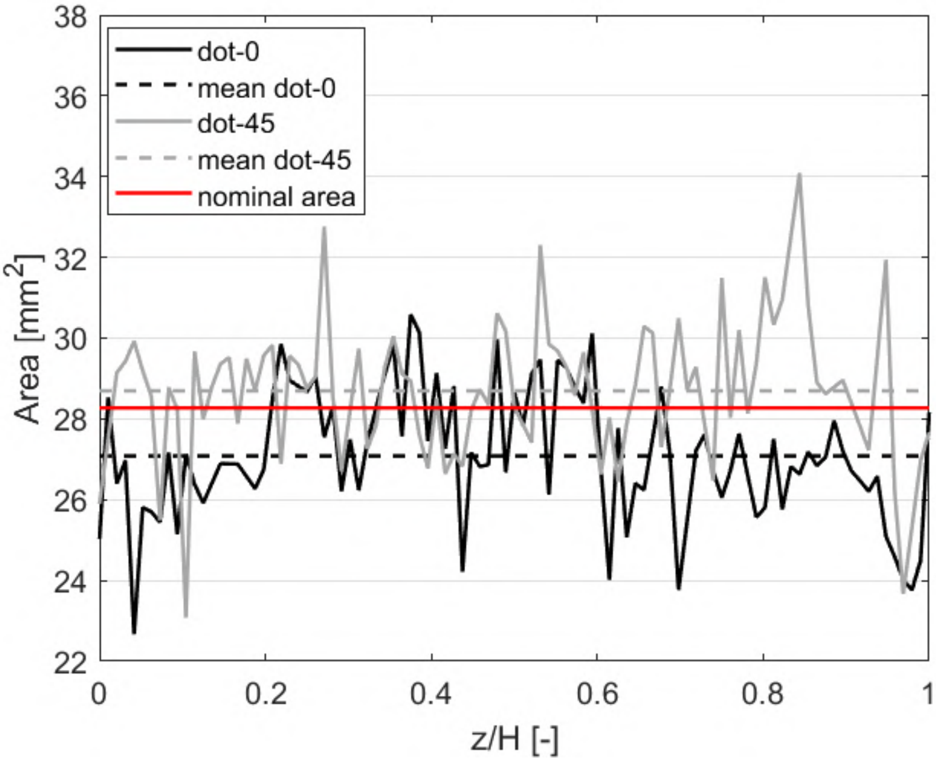

Figure 9: Graphical representation of the variation of the cross-sectional area A(z) along the longitudinal axis.

Then, the statistical distribution of the real cross-sectional area was computed and normalized in terms of mean value ($A_{real}(z)/A_{mean}$). For both specimens, Normal and Lognormal best-fit distributions were also computed. In both cases, the two distributions fit well the data. The standard deviation values (which, in case of normalized distributions, correspond to the coefficient of variation) resulted equal to 0.06 for both dot-0 and dot-45 bars.

The average real diameter $d_{real}(z)$ resulting from the analysis of the 3D-scan acquisition for the dot-0 bar resulted equal to 5.87 mm, with a coefficient of variation equal to 3%. Regarding the dot-45 bar, the mean diameter resulted equal to 6.05 mm, with a coefficient of variation equal to 3%. Again, the results are in line with findings reported in the work by Silvestru et al. [35] which evidenced standard deviation values between 0.13 and 0.21 mm (for a nominal diameter of 8 mm).

The out-of-roundness was estimated by computing the ratio between the real diameter (d_{real}) computed according to Section 3.4 and each of the two dimensions of the circumscribed rectangle (L_x, L_y). For the dot-0 bar, the average values of the ratios L_x/d_{real} and L_y/d_{real} resulted equal to 1.03 and 0.99, respectively, with a coefficient of variation of 2% for both of them. For the dot-45 bar, the average values of the ratios L_x/d_{real} and L_y/d_{real} resulted equal to 1.01 and 1.00, respectively, with a coefficient of variation of 2% for both of them. Thus, the results confirmed that the real cross-sections can be approximated to a circular shape.

Figure 10a displays the real longitudinal axis of the two WAAM bars, i.e. dot-0 (blue line) and dot-45 (red line). The eccentricity (e) of the bars were computed in terms of modulus of the coordinates of the real centroid $C_{real}(z)=(C_{real,x},C_{real,y})$ as follows: $e=\sqrt{C_{real,x}{}^2+C_{real,y}{}^2}$. For the dot-0 bar, the mean value (e_{mean}) and standard deviation (σ_e) of e (over a height of 250 mm) resulted equal to e_{mean} = 0.43 mm and σ_e = 0.23 mm (coefficient of variation of 0.53), with a maximum value equal to e_{max} = 0.92 mm (for a ratio e_{max}/H equal to 0.46%). For the dot-45 bar, the mean value and the standard deviation of e (over a height of 200 mm) resulted equal to e_{mean} = 0.55 mm and σ_e = 0.26 mm (coefficient of variation of 0.48), with e_{max} = 1.12 mm (for a ratio e_{max}/H equal to 0.58%). The comparison of values of the three main descriptors of the eccentricity (i.e. e_{max}, e_{mean}, σ_e) indicates that the dot-45 bar has higher irregularity (+15-30%) with respect to the dot-0. Similar findings were also reported in the work by [35] which evidenced a much rougher surface in case of 45° built angle. The larger irregularity of the dot-45 bar could have a detrimental effect on the mechanical parameters of bars printed with higher build angles. The values of e_{max} for the investigated dot-0 and dot-45 specimens are also indicated in Figure 10a with a star.

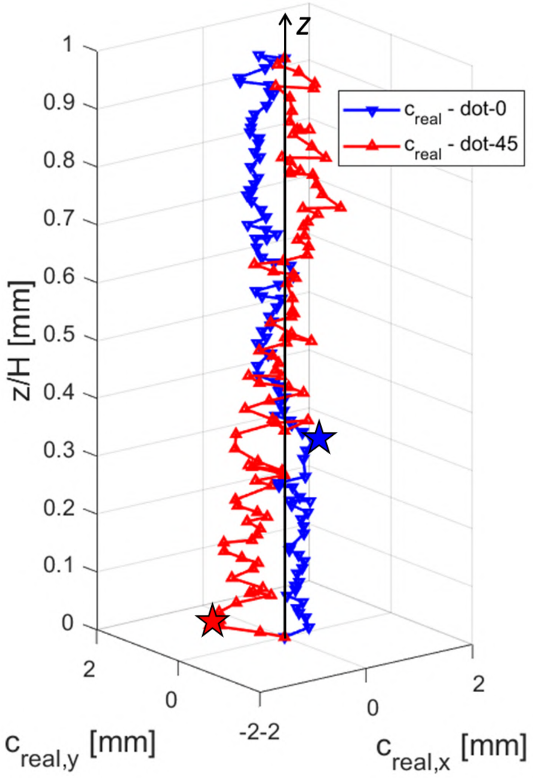

(a)

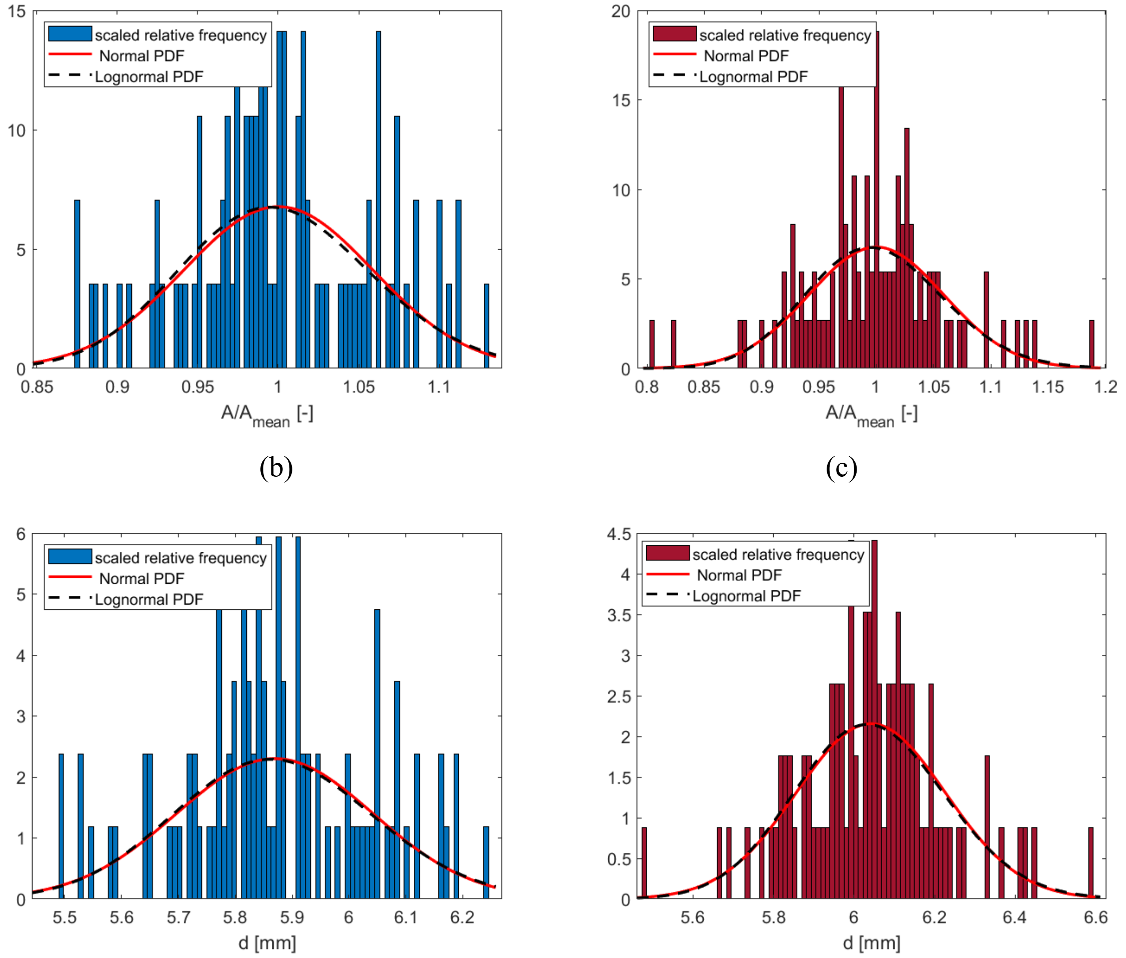

(b) (c)

(d) (e)

Figure 10: Geometrical characterization of WAAM bars printed with different build angles: (a) comparison of longitudinal eccentricity (blue – dot-0, red – dot-45); frequency distribution of normalized cross-sectional area (b) for dot-0, (c) for dot-45; frequency distribution of diameters (d) for dot-0 (e) for dot-45.

4.4 Tensile and hardness data

The tensile tests were performed on a total of 29 specimens (10 dot-0 specimens, 10 dot-10 specimens and 9 dot-45 specimens). Figure 11 presents the effective stress-strain curve of WAAM bars and a zoom of them (for strain values lower than 1% and stress values lower than 400 MPa). Effective stress values σ_{eff} were computed as the ratio between the tensile force acting on the specimen and its effective cross-sectional area (according to Eq.1). Effective strains were computed according to Eq. 2 and considering a gauge length of 50 mm. Overall, for all three inclinations considered, a significant inherent variability in the tensile response can be detected for each single orientation. Dot-0 and dot-10 specimens presented ultimate tensile strength values up to 600 MPa and elongation to failure up to 40%. On the other hand, dot-45 specimens presented ultimate tensile strength values up to 480 MPa and elongation to failure values up to 35%. All three orientations registered very large post-yielding hardening behavior until rupture. From a closer look at the first part of the tensile tests (deformation values less than 1%) (Figures 11 b,d,f), the 0.2% proof stress values were around 200-250 MPa for all three inclinations.

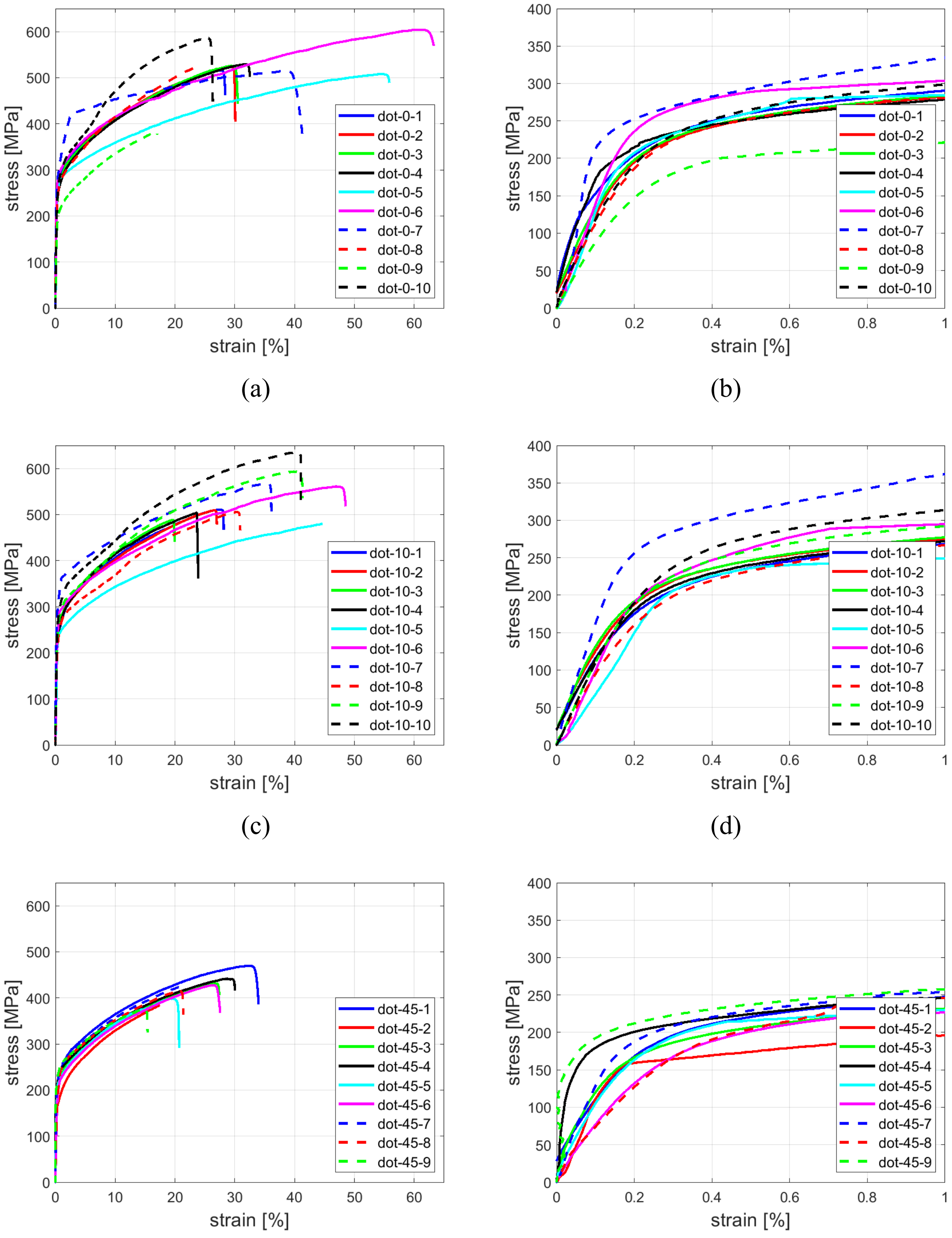

(a) (b)

(c) (d)

(e) (f)

Figure 11: Effective stress-strain curves for tensile tests on WAAM bars: full curve and a zoom of them (up to 1% strain) for specimens with (a,b) dot-0, (c,d) dot-10 and (e,f) dot-45.

Table 4 collects the values of the key effective mechanical parameters (means +/- standard deviations), in terms of Young's modulus (E), 0.2% proof stress ($R_{p,02}$), ultimate tensile strength (UTS and elongation to failure ($A_{\%}$) according to ISO 6892-1 [57]. Values of yield-to-tensile strength ratio ($R_{p0.2}/UTS$) and element's ductility ($\mu_e = \frac{\varepsilon_{eff,u}}{\varepsilon_{eff,Rp02}} = \frac{A_{\%}}{\varepsilon_{eff,Rp02}}$) are also reported. In order to accurately evaluate the Young's modulus values overcoming the experimental noise typical of the effective stress-strain curves, an ordinary least squares regression (OLSR) analysis was employed, as proposed by [67] and also adopted in [25,40].

Table 4: Key effective mechanical parameters from tensile tests on WAAM bars.

Specimen ID	**E [GPa]**	**$R_{p0.2}$ [MPa]**	**UTS [MPa]**	**$A_{\%}$ [%]**	**$R_{p0.2}$/ UTS [-]**	**μ_e [-]**
dot-0	133 ± 27	243 ± 20	524 ± 56	35 ± 14	0.47 ± 0.03	93 ± 42
dot-10	108 ± 19	245 ± 21	536 ± 49	34 ± 9	0.46 ± 0.03	79 ± 21
dot-45	98 ± 28	208 ± 20	419 ± 29	24 ± 6	0.50 ± 0.05	55 ± 14

Overall, the average value of all the key effective mechanical parameters decrease with increasing build angle. As far as Young's modulus is concerned, the specimens present significantly low values (between 100 and 140 GPa) with a very large scatter. Values of 0.2% proof stress and ultimate tensile strength are instead comparable to the standard values for structural steel. Elongation at rupture values are between 25% and 35% with very large scatter for all three build angles. The ductility of the element has values ranging between 50 to 100 with, again, very large scatter for all three build angles. Hardness results (HV_1) are reported in Figure 12, as average values measured on the longitudinal and transverse metallographic sections of all investigated build angles. By considering standard deviations, hardness evaluated on longitudinal sections (along z-axis), thus parallel to the tensile load direction, can be considered comparable among dot-0, dot-10 and dot-45 bars. On the other hand, for all build angles tested, hardness measured on transverse section (perpendicular to the z-axis) was lower than longitudinal one. The slight difference between the longitudinal and transverse sections is possibly related to the difference in the microstructural features discussed in Section 4.2. Specifically, both optical and FEG-SEM microscopy showed an anisotropy in the microstructure due to the additive process, evident if the morphology of the δ-ferrite (whose hardness and strength are slightly higher than austenite) is concerned. Furthermore, a modest decrease in the average hardness value was observed for bars printed with 10° and 45° build angle, if compared to 0° ones. Consequently, the overall hardness of 0° bars (287 HV_1) was higher than 10 and 45° ones (257 and 264 HV_1, respectively). However, the difference among the three build angles tested is very narrowed.

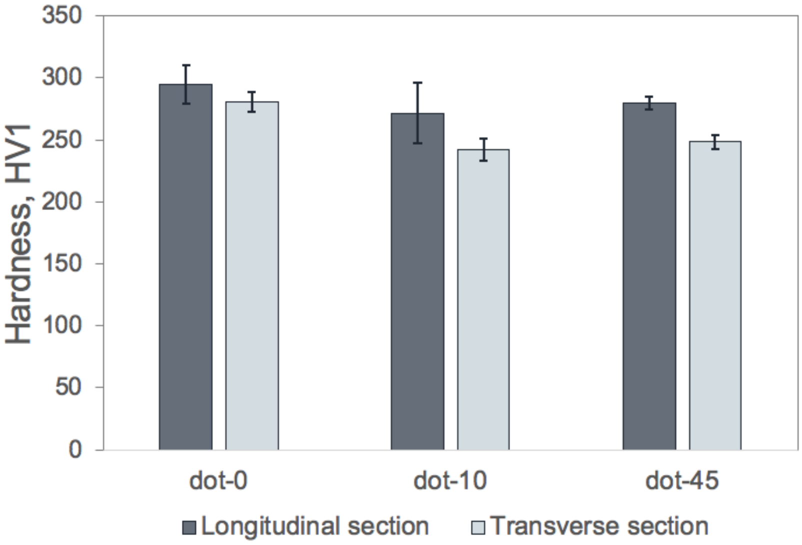

Figure 12: Hardness measurements. (HV_1) performed on longitudinal and transverse section of WAAM bars.

4.5 Fracture surfaces

Fracture surfaces were initially observed at low magnification by means of a 3D digital microscope. In order to delineate the fracture path, micrographs in Figure 13 show the view along *z*-axis of representative dot-0, dot-10, and dot-45 specimens (Figure 13 a,b,c), and the corresponding metallographic sections (Figure 13 d,e,f). From the analyses in Figure 13 it is evident that, for all the tested build angles, fracture occurred along a direction inclined by 45° to the applied tensile load (i.e. longitudinal *z*-axis), consistent with the plane of maximum shear stress. By referring to the layer boundaries, underlined by the yellow dashed lines in the figure, dot-45 specimens were characterized by the most unfavorably orientation with respect to the plane of maximum shear stress. In fact, as also discussed above, the layer boundaries of dot-45 were approximately oriented at 45° to the *z*-axis. This outcome contributes to further justify the mechanical properties of dot-45 specimens, lower than dot-0 and dot-10 especially in terms of tensile strength and elongation. By recalling the results of microstructural analyses, the interlayer region is characterized by a change in the morphology of the columnar dendritic structure, as coarsening of the microstructure occurs due to the deposition of the following droplet (Figure 7a). In addition, it can be assumed that minor localized oxidation or contamination phenomena occurred, even if the surface of the molten metal is protected by a shielding gas during the deposition. This assumption is supported by the globular particles, presumably related to non-metallic inclusions, that were detected in the microstructure (Figure 8).

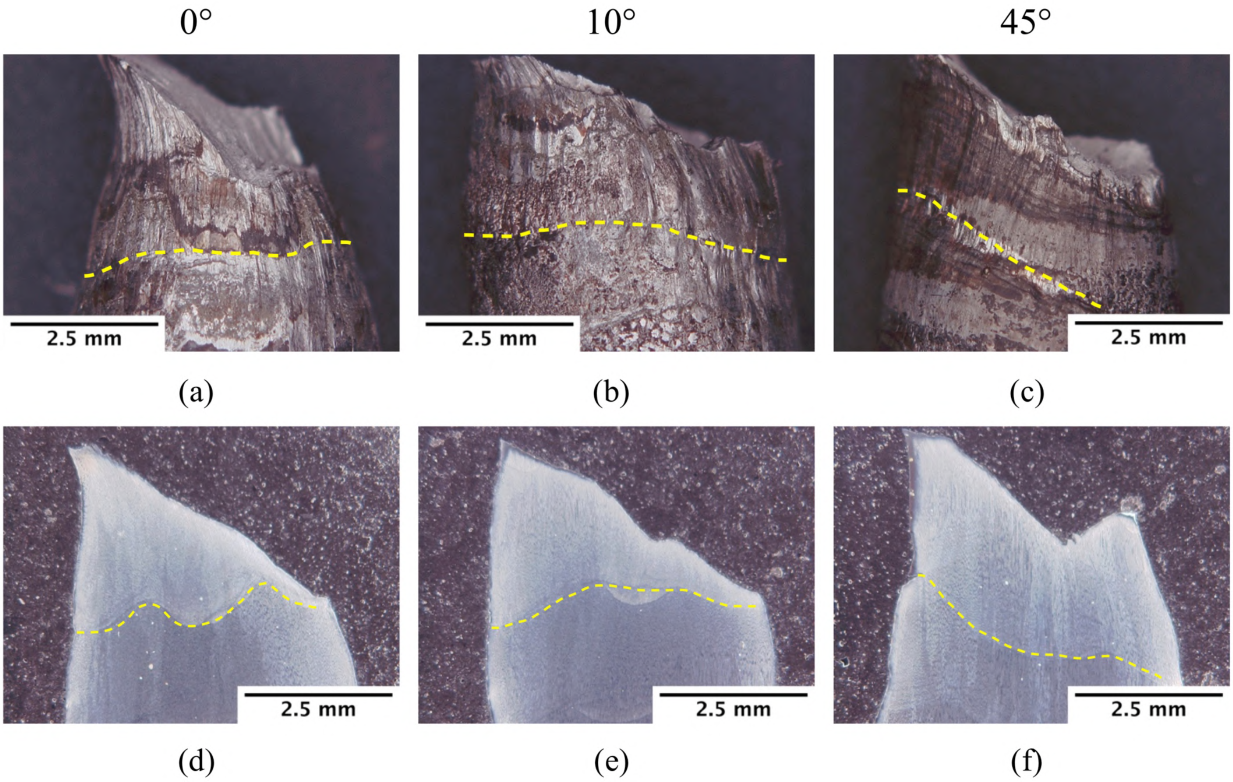

Figure 13: Analyses of fracture surfaces by means of 3D digital microscopy: a), b), c) longitudinal view and d), e), f) metallographic sections of 0°, 10° and 45° WAAM bars.

The same globular particles were markedly detected on fracture surfaces of all samples, suggesting that they had a major role in determining the mechanical performances of the WAAM bars. In fact, fracture surfaces were observed at both low and high magnification by means of FEG-SEM (Figure 14). A general view of fracture surfaces can be appreciated in low magnification analyses (Figure 14 a,b,c), where a ductile fracture characterized by dimples can be observed for all specimens, regardless the build angle. A more detailed insight into dimples morphology was obtained at higher magnification (Figure 14 d,e,f). As a consequence of the very fine microstructure resulting from the WAAM process, dimples size was in the order of few micrometers. No trace of a preferred orientation among samples was evidenced. It is known that dimples form due to microvoids nucleation, growth and coalescence in correspondence of hard second phases, such as non-metallic inclusions that strongly contribute to the ductile fracture [68]. In fact, globular sub-micrometric particles, consistent with the ones observed in Section 4.2, were detected inside dimples on WAAM bars. A detail of a globular particle is given in Figure 14g, with the corresponding semi-quantitative chemical analysis performed by EDS, that confirmed the presence of O, Mn, S and Si. As already discussed, oxygen compounds on fracture surfaces can be related to oxidation phenomena occurring during the WAAM process and could indeed justify the lower elongation at fracture exhibited by WAAM bars compared to the conventional wrought material, as well as the scatter showed in the elongation results.

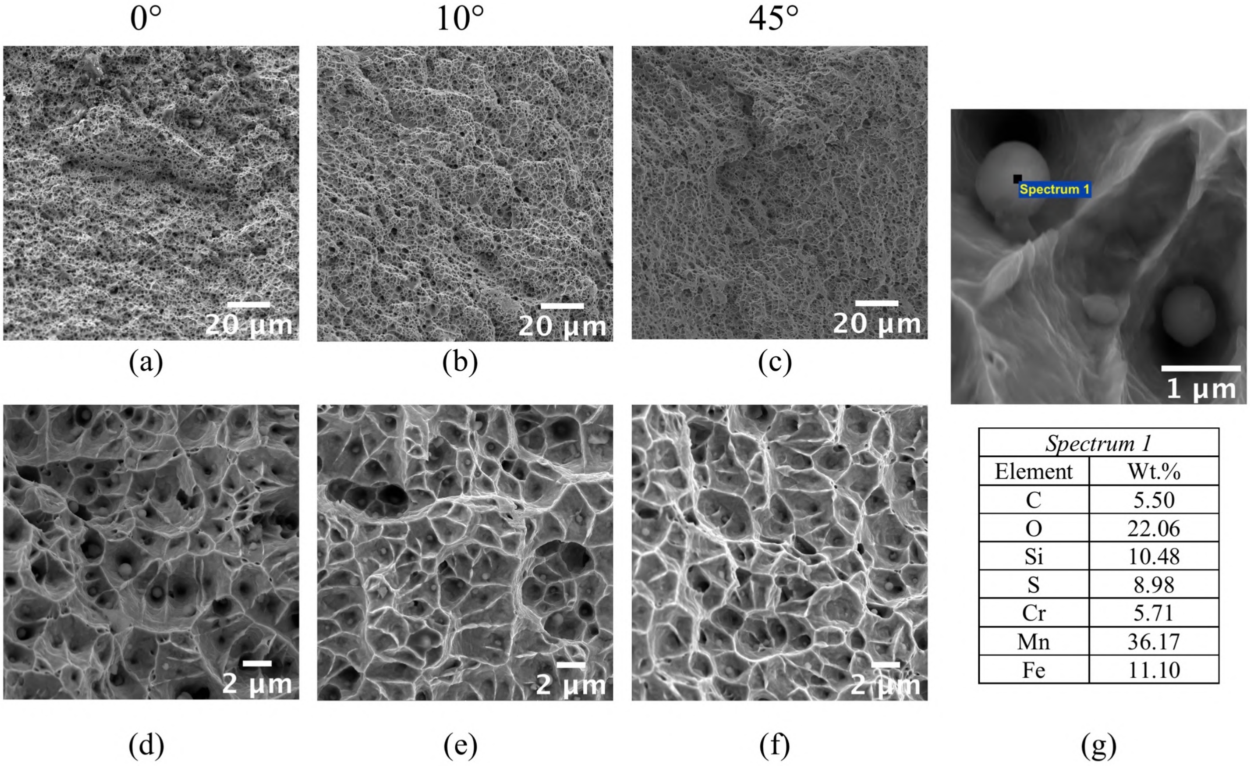

Spectrum 1	
Element	Wt.%
C	5.50
O	22.06
Si	10.48
S	8.98
Cr	5.71
Mn	36.17
Fe	11.10

Figure 14: FEG-SEM analyses of fracture surfaces: a), b) c) low and d), e), f) high magnification of dot-0, dot-10 and dot-45 bars; (g) microanalysis on globular particles (probably oxides) found inside dimples on the fracture surfaces of WAAM bars.

5. Interpretation of the mechanical response

5.1 Variability of the geometrical irregularities

Table 5 reports the ratios between the average effective/nominal diameters and cross-sectional areas (d_{eff}/d_n and A_{eff}/A_n) together with the coefficients of variation of the effective diameters for the different build angles. The ratios of the diameter values are between 0.95 and 1.07, while the COV values are equal to 5%, independently from the specific build angle. These results are also in line with the findings reported by Silvestru et al. [35] which evidenced discrepancies between average and nominal diameters in the range of +/-5%.

Overall, the detrimental effect of the higher build angles on the geometrical irregularities (as estimated for the dot-45 specimens) could be associated to the lower surface tension of the molten pool, which is used to counter gravity and thus avoid overhang limitations. Thus, in order to overcome this issue, future studies should be devoted to fine tune the process parameters, with specific regard to the heat input.

Table 5: Variability of the specimen-to-specimen geometrical irregularities (mean and standard deviation).

	Specimen-to-specimen geometrical variability	
Specimen ID	**d_{eff}/d_n [-]**	**A_{eff}/A_n [-]**
dot-0	0.99 ± 0.05	0.98 ± 0.10
dot-10	0.95 ± 0.05	0.91 ± 0.09
dot-45	1.07 ± 0.05	1.14 ± 0.10

Table 6 summarizes the main results obtained from the inherent geometrical characterization of the dot-0 and dot-45 3D-scanned bars in terms of: (i) ratios between the real and effective cross-sectional area (A_{real}/A_{eff}) and (ii) diameter (d_{real}/d_{eff}), (iii) discrepancy between real and nominal diameter (d_{real}/d_n), (iv) out-of-roundness parameters (L_x/d_{real} and L_y/d_{real}) and (v) lack-of-straightness parameter (e/H). It can be noted that the COV values are around 2-3% for the diameter and out-of-roundness parameter, around 6% for the cross-sectional area, and around 10-12% for the lack-of-straightens parameters.

The overall variability resulting from specimen-to-specimen and inherent variability is one important source of variability of the key effective mechanical parameters. For instance, the overall COV of the cross-sectional area can be estimated through the well-known SRSS combination rule, resulting in a value of around 12%.

In general, the geometrical parameters here studied (i.e. diameter variability, eccentricity) could be used as reference for a methodology aimed at evaluating and further classifying the printing quality of WAAM bars realized by various providers with different sets of process parameters.

Table 6: Variability of the inherent geometrical irregularities (mean and standard deviation)

	Inherent geometrical irregularities					
Specimen ID	**A_{real}/A_{eff} [-]**	**d_{real}/d_{eff} [-]**	**L_x/d_{real} [-]**	**L_y/d_{real} [-]**	**d_{real}/d_n [-]**	**e/H [%]**
dot-0	0.98 ± 0.06	0.99 ± 0.03	1.02 ± 0.02	0.99 ± 0.02	0.98 ± 0.03	0.22 ± 0.12
dot-45	0.99 ± 0.06	0.99 ± 0.03	1.01 ± 0.03	1.00 ± 0.02	1.01 ± 0.03	0.28 ±0.10

5.2 *Variability of the key effective mechanical parameters*

Table 7 reports the values of the coefficient of variation (COV) registered for the key effective mechanical parameters, considering the three different build angles. The values allow to make some interesting observation regarding the variability of such parameters. Young's modulus values exhibited large COV, in the range of 20-30%. Such values are in line with those exhibited by the as-built specimens cut from plates and printed with the same wire [25] and are mainly caused by the inherent geometrical irregularities of the specimens (both cross section area and lack of straightness). 0.2% proof stress and ultimate tensile strength variabilities are between 8-12%. As expected, such variability is very close to the overall cross-sectional area variability (COV estimate equal to 12%). Elongation at rupture and element's ductility exhibit very large COV values, in the range of 25-45%, which are influenced by all the geometrical variabilities. The high sensitivity of these parameters on all the geometrical irregularities is in line with the observations provided in Section 2.

Table 7: Variability of the key effective mechanical parameters (COV).

	Effective mechanical parameter variability

Specimen ID	**E**	**$R_{p0.2}$**	**UTS**	**$A_{\%}$**	**μ_e**
dot-0	22%	11%	12%	39%	45%
dot-10	18%	9%	9%	33%	27%
dot-45	28%	8%	7%	26%	26%

Figure 15 and Table 8 compare the key effective mechanical parameters for the three build angles investigated on WAAM bars. Reference to traditional values of the key mechanical parameters of 304L stainless steel according to European building code [58] (red dotted line) and the results obtained for specimens cut transversally from WAAM-produced 304L stainless steel plates (presented in [38]) are also provided.

Young's modulus values are much lower than the conventional 304L stainless steel (140 to 100 GPa vs. 200 GPa). Values of 0.2% proof stress are within the ranges provided by Eurocode 3 [58] for conventional 304L stainless steel. Similar results are registered for ultimate tensile strength values, with the exception of dot-45 specimens, for which a value of around 420 MPa is computed on average, lower than the recommended ranges in [58] of 500-520 MPa for 304L steel. The lower tensile strength of dot-45 specimens can be associated to both the geometrical irregularities (see Section 4.3) and the unfavorable orientation of the layer boundaries (see Section 4.2) to the tensile load, as also confirmed by their lower elongation.

With reference to the key effective mechanical parameters extracted from WAAM 304L stainless steel plates (WAAM-T, see e.g. [25,37,38]), the values of Young's modulus and elongation at rupture are in line with those reported in this study. The low stiffness is indeed related to the texture formed due to the epitaxial grain growth evidenced by microstructural analysis performed on bars (see Section 4.2) and investigated more in details on plates (see e.g. [25,42]).

On the other hand, 0.2% proof stress values reported for WAAM bars are significantly lower than WAAM-T (of around 250 MPa vs. 350 MPa). Slightly lower values are also registered for ultimate tensile strength values (of around 500 MPa vs. 600 MPa).

With reference to the elongation and ductility, it should be noticed that a high deviation from the average value was evidenced. In addition to the previously discussed geometric variability, it should be also taken into account that the nonmetallic inclusions and microporosities observed during microstructural and fractographic analyses, strongly influence the mechanical behavior, especially in terms of ductility and elongation.

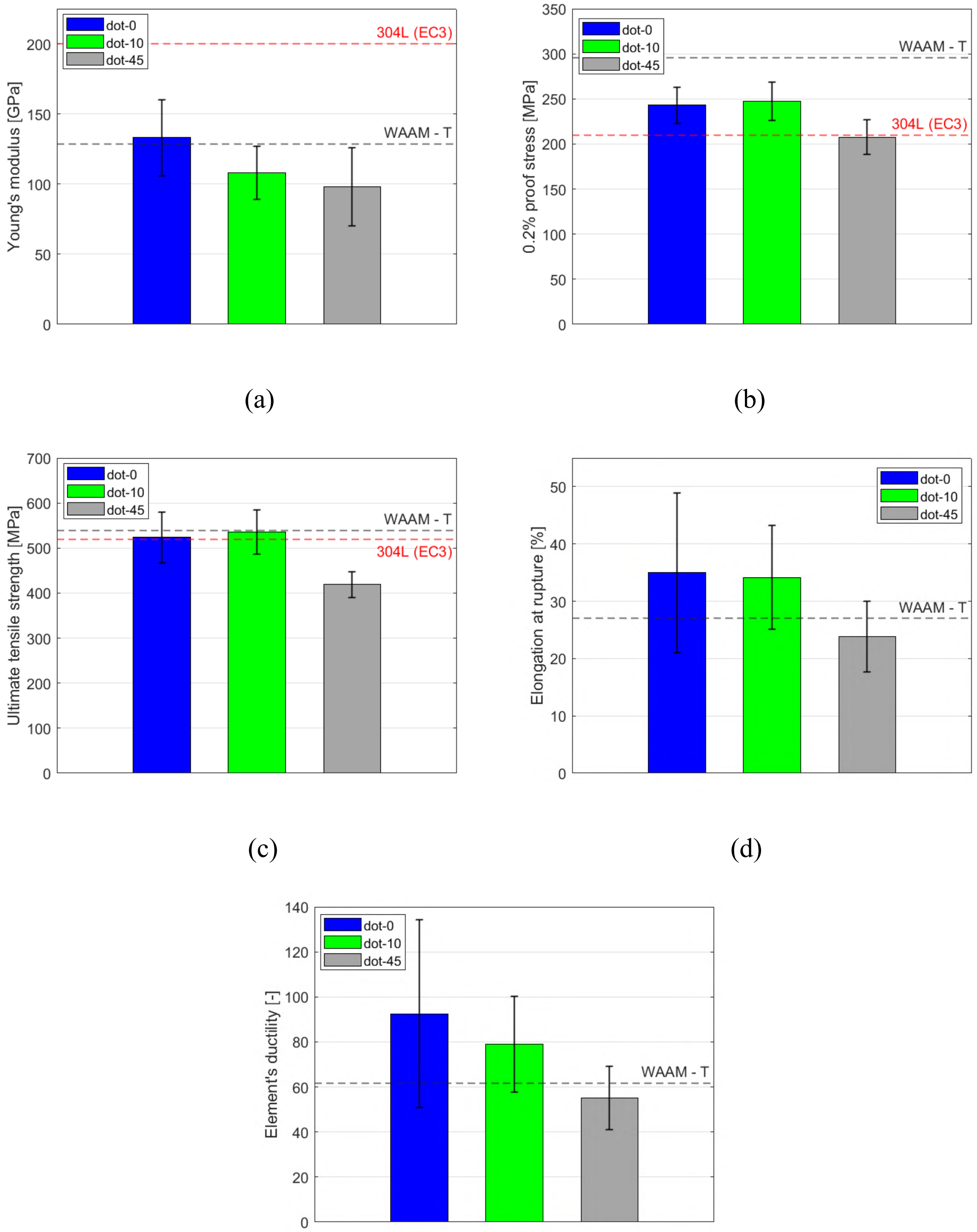

(a) (b)

(c) (d)

(e)

Figure 15: Results of the tensile tests on WAAM dot-by-dot bars printed at different angles: (a) Young's modulus; (b) 0.2% proof stress; (c) ultimate tensile strength; (d) elongation at rupture; (e) element's ductility. Reference values for conventional 304L stainless steel (from EC3) and results from WAAM specimens cut transversally from plates (WAAM-T) (Ref. [38]*) are also added.*

From the comparison between the specimens printed with different build angles (as also provided in Table 8), overall the specimens printed at low build angles (dot-0 and dot-10) register good strength properties (in terms of 0.2% proof stress and ultimate tensile strength) in line with conventional 304L stainless steel. Values of Young's modulus, elongation at rupture and element's ductility registered instead the highest influence of the build angle. The detrimental effect of the higher build angle in the elongation at rupture and element's ductility might be due to the higher geometrical irregularities, which could influence the ductile behavior after yielding, as also presented in Section 2.

Table 8: Relative ratios of the key mechanical parameters with respect to the build angle.

	Influence of built angle				
Relative ratio	**E** [-]	**$R_{p0.2}$** [-]	**UTS** [-]	**$A_{\%}$** [-]	**μ_e** [-]
dot-10/dot-0	0.78	0.98	1.00	1.00	0.85
dot-45/dot-0	0.69	0.82	0.78	0.64	0.59

All results obtained from the geometrical and mechanical characterization provides a body of knowledge that can be then used in further study to calibrate ad-hoc partial factors for the structural design of WAAM lattice structures. Clearly each set of partial factors is highly correlated to the specific printing process characterized by a given set of printing parameters.

Conclusions

The study presents the first results of an extensive experimental work devoted to assess the mechanical response of stainless steel bars printed with Wire-and-Arc Additive Manufacturing (WAAM). In particular, the work focuses on the mechanical response under tensile loading of as-built bars in terms of effective mechanical parameters, with the aim of studying: (i) the influence of the geometrical irregularities proper of the printing process on the mechanical response under tension, (ii) the effect of increasing build angle in the key effective mechanical parameters. Microstructural analysis and detailed geometrical characterization of selected specimens were also carried out for a better interpretation of the results of the tensile tests.

The main results are summarized as follows:

- Chemical composition of the printed bars complied with the requirements for the AISI 304L austenitic stainless steel.
- Microstructural characterization revealed a microstructure directly affected by the deposition process, consisting of successive layers of solidified material, large epitaxial grains crossing over layers and a fine columnar dendritic substructure within grains. For all build angles (0°, 10° and 45°) grains and substructure were strongly oriented along the longitudinal axis of the bars. On the other hand, the inclination of layer boundaries to the longitudinal axis increased with the build angle, being maximum for the 45° built bars.
- The results of the geometrical characterization through 3D scanning acquisition on the specimens printed with three different build angles (at 0°, 10° and 45°) revealed a quite uniform specimen-to-specimen variability of the effective diameters and cross-sectional areas with coefficient of variations of around 5% and 10% respectively, independently from the build angles. On the contrary, a detrimental effect of the build angle is observed in terms of increased lack of straightness when comparing specimens printed at 0° and 45° (+30% on the average value and +15% on the maximum value).
- The results of the tensile tests revealed a significant inherent variability (e.g. for a fixed build angle) of all the key effective mechanical parameters with coefficient of variation values ranging from 10% for the yield and ultimate strength parameters up to 30-40% for the parameters associated to the deformation capacity (Young's modulus, elongation at rupture and ductility). Furthermore, the specimens printed at 45° build angle had reduced values of all the key effective mechanical parameters (-20÷35%) with respect to those printed at 0° or 10°. In particular, severely reduced values of element's ductility and Young's modulus were

registered. Reasonings to this can be found in the higher geometrical irregularities, which alter the mechanical response of bars.

- Detailed inspection of the fracture surfaces revealed a ductile fracture behavior in all the investigated specimens. In addition, fracture occurred along the direction of maximum shear stress, tilted at 45° to the longitudinal axis of bars. In this view, bars printed with a 45° build angles revealed to be the most disadvantaged ones.

Overall, the results show a significant variability of the effective mechanical parameters on the inherent geometrical irregularities with a detrimental effect of large build angles on all the geometrical irregularities (especially the lack of straightness) and on the mechanical behavior. These results confirm the need of ad-hoc calibrated partial safety factors for structural design that could properly account for both the inherent geometrical and mechanical variabilities associated to a specific set of WAAM printing parameters.

In this regard, an improved printing process would lead to reduced geometrical discrepancies and, thus, superior mechanical properties, especially in terms of deformation capacity.

Acknowledgements

The support of Dutch company MX3D held in Amsterdam is gratefully acknowledged for giving the additive-manufactured elements tested.

Declarations

Funding

Not applicable.

Declaration of Competing Interest

The authors declare that they have no known competing financial interests or personal relationships that could have appeared to influence the work reported in this paper.

Data availability

The raw/processed data required to reproduce these findings cannot be shared at this time as the data also forms part of an ongoing study.

CRediT authorship contribution statement

Vittoria Laghi: Conceptualization, Methodology, Validation, Investigation, Writing – Original Draft.
Michele Palermo: Methodology, Visualization, Writing – Review & Editing.
Lavinia Tonelli: Validation, Investigation, Writing – Original Draft.
Giada Gasparini: Writing – Review & Editing.
Valentina Alena Girelli: Investigation.
Lorella Ceschini: Validation, Writing – Review & Editing.
Tomaso Trombetti: Supervision.

References

[1] K.S. Derekar, A review of wire arc additive manufacturing and advances in wire arc additive manufacturing of aluminium, Mater. Sci. Technol. (United Kingdom). 34 (2018) 895–916. https://doi.org/10.1080/02670836.2018.1455012.

[2] T.A. Rodrigues, V. Duarte, R.M. Miranda, T.G. Santos, J.P. Oliveira, Current status and perspectives on wire and arc additive manufacturing (WAAM), Materials (Basel). 12 (2019).

https://doi.org/10.3390/ma12071121.

[3] C. Buchanan, L. Gardner, Metal 3D printing in construction: A review of methods, research, applications, opportunities and challenges, Eng. Struct. 180 (2019) 332–348. https://doi.org/10.1016/j.engstruct.2018.11.045.

[4] C. V. Haden, G. Zeng, F.M. Carter, C. Ruhl, B.A. Krick, D.G. Harlow, Wire and arc additive manufactured steel: Tensile and wear properties, Addit. Manuf. 16 (2017) 115–123. https://doi.org/10.1016/j.addma.2017.05.010.

[5] L. Ji, J. Lu, C. Liu, C. Jing, H. Fan, S. Ma, Microstructure and mechanical properties of 304L steel fabricated by arc additive manufacturing, MATEC Web Conf. 128 (2017). https://doi.org/10.1051/matecconf/201712803006.

[6] A.S. Yildiz, K. Davut, B. Koc, O. Yilmaz, Wire arc additive manufacturing of high-strength low alloy steels : study of process parameters and their influence on the bead geometry and mechanical characteristics, (2020).

[7] P. Moore, A. Addison, M. Nowak-Coventry, Mechanical properties of wire plus arc additive manufactured steel and stainless steel structures, Weld. World. 63 (2019) 1521–1530. https://doi.org/10.1007/s40194-019-00775-4.

[8] M. Ghaffari, A. Vahedi Nemani, M. Rafieazad, A. Nasiri, Effect of Solidification Defects and HAZ Softening on the Anisotropic Mechanical Properties of a Wire Arc Additive-Manufactured Low-Carbon Low-Alloy Steel Part, Jom. 71 (2019) 4215–4224. https://doi.org/10.1007/s11837-019-03773-5.

[9] Y. Fu, H. Zhang, G. Wang, H. Wang, Investigation of mechanical properties for hybrid deposition and micro-rolling of bainite steel, J. Mater. Process. Technol. 250 (2017) 220–227. https://doi.org/10.1016/j.jmatprotec.2017.07.023.

[10] M. Eriksson, M. Lervåg, C. Sørensen, A. Robertstad, B.M. Brønstad, B. Nyhus, R. Aune, X. Ren, O.M. Akselsen, Additive manufacture of superduplex stainless steel using WAAM, MATEC Web Conf. 188 (2018) 1–8. https://doi.org/10.1051/matecconf/201818803014.

[11] M. Dinovitzer, X. Chen, J. Laliberte, X. Huang, H. Frei, Effect of wire and arc additive manufacturing (WAAM) process parameters on bead geometry and microstructure, Addit. Manuf. 26 (2019) 138–146. https://doi.org/10.1016/j.addma.2018.12.013.

[12] W. Wu, J. Xue, L. Wang, Z. Zhang, Y. Hu, C. Dong, Forming process, microstructure, and mechanical properties of thin-walled 316L stainless steel using speed-cold-welding additive manufacturing, Metals (Basel). 9 (2019). https://doi.org/10.3390/met9010109.

[13] X. Zhang, Q. Zhou, K. Wang, Y. Peng, J. Ding, J. Kong, S. Williams, Study on microstructure

and tensile properties of high nitrogen Cr-Mn steel processed by CMT wire and arc additive manufacturing, Mater. Des. 166 (2019) 107611. https://doi.org/10.1016/j.matdes.2019.107611.

[14] M. Rafieazad, M. Ghaffari, A. Vahedi Nemani, A. Nasiri, Microstructural evolution and mechanical properties of a low-carbon low-alloy steel produced by wire arc additive manufacturing, Int. J. Adv. Manuf. Technol. 105 (2019) 2121–2134. https://doi.org/10.1007/s00170-019-04393-8.

[15] J. Wang, Z. Pan, Y. Wang, L. Wang, L. Su, D. Cuiuri, Y. Zhao, H. Li, Evolution of crystallographic orientation, precipitation, phase transformation and mechanical properties realized by enhancing deposition current for dual-wire arc additive manufactured Ni-rich NiTi alloy, Addit. Manuf. 34 (2020) 101240.

[16] L. Sun, F. Jiang, R. Huang, D. Yuan, C. Guo, J. Wang, Anisotropic mechanical properties and deformation behavior of low-carbon high-strength steel component fabricated by wire and arc additive manufacturing, Mater. Sci. Eng. A. 787 (2020) 139514. https://doi.org/10.1016/j.msea.2020.139514.

[17] B.A. Szost, S. Terzi, F. Martina, D. Boisselier, A. Prytuliak, T. Pirling, M. Hofmann, D.J. Jarvis, A comparative study of additive manufacturing techniques: Residual stress and microstructural analysis of CLAD and WAAM printed Ti-6Al-4V components, Mater. Des. 89 (2016) 559–567. https://doi.org/10.1016/j.matdes.2015.09.115.

[18] R. Biswal, X. Zhang, A.K. Syed, M. Awd, J. Ding, F. Walther, S. Williams, Criticality of porosity defects on the fatigue performance of wire + arc additive manufactured titanium alloy, Int. J. Fatigue. 122 (2019) 208–217. https://doi.org/10.1016/j.ijfatigue.2019.01.017.

[19] F. Veiga, A. Gil Del Val, A. Suárez, U. Alonso, Analysis of the Machining Process of Titanium Ti6Al-4V Parts Manufactured by Wire Arc Additive Manufacturing (WAAM), Materials (Basel). 13 (2020). https://doi.org/10.3390/ma13030766.

[20] C. Zhang, Y. Li, M. Gao, X. Zeng, Wire arc additive manufacturing of Al-6Mg alloy using variable polarity cold metal transfer arc as power source, Mater. Sci. Eng. A. 711 (2018) 415–423. https://doi.org/10.1016/j.msea.2017.11.084.

[21] E.M. Ryan, T.J. Sabin, J.F. Watts, M.J. Whiting, The influence of build parameters and wire batch on porosity of wire and arc additive manufactured aluminium alloy 2319, J. Mater. Process. Technol. 262 (2018) 577–584. https://doi.org/10.1016/j.jmatprotec.2018.07.030.

[22] Z. Qi, B. Cong, B. Qi, G. Zhao, J. Ding, Properties of wire + arc additively manufactured 2024 aluminum alloy with different solution treatment temperature, Mater. Lett. 230 (2018) 275–

278. https://doi.org/10.1016/j.matlet.2018.07.144.

[23] M. Köhler, S. Fiebig, J. Hensel, K. Dilger, Wire and arc additive manufacturing of aluminum components, Metals (Basel). 9 (2019) 1–9. https://doi.org/10.3390/met9050608.

[24] J. V. Gordon, C. V. Haden, H.F. Nied, R.P. Vinci, D.G. Harlow, Fatigue crack growth anisotropy, texture and residual stress in austenitic steel made by wire and arc additive manufacturing, Mater. Sci. Eng. A. 724 (2018) 431–438. https://doi.org/10.1016/j.msea.2018.03.075.

[25] V. Laghi, M. Palermo, G. Gasparini, V.A. Girelli, T. Trombetti, On the influence of the geometrical irregularities in the mechanical response of Wire-and-Arc Additively Manufactured planar elements, J. Constr. Steel Res. 178 (2021) 106490. https://doi.org/10.1016/j.jcsr.2020.106490.

[26] P. Kyvelou, H. Slack, D. Daskalaki Mountanou, M.A. Wadee, T. Ben Britton, C. Buchanan, L. Gardner, Mechanical and microstructural testing of wire and arc additively manufactured sheet material, Mater. Des. 192 (2020) 108675. https://doi.org/10.1016/j.matdes.2020.108675.

[27] L. Gardner, P. Kyvelou, G. Herbert, C. Buchanan, Testing and initial verification of the world's first metal 3D printed bridge, J. Constr. Steel Res. 172 (2020). https://doi.org/10.1016/j.jcsr.2020.106233.

[28] T. Feucht, J. Lange, 3-d-printing with steel: Additive manufacturing of connection elements, Adv. Eng. Mater. Struct. Syst. Innov. Mech. Appl. - Proc. 7th Int. Conf. Struct. Eng. Mech. Comput. 2019. (2019) 419–424. https://doi.org/10.1201/9780429426506-75.

[29] T. Feucht, J. Lange, B. Waldschmitt, A.-K. Schudlich, M. Klein, M. Oechsner, Welding Process for the Additive Manufacturing of Cantilevered Components with the WAAM BT - Advanced Joining Processes, in: L.F.M. da Silva, P.A.F. Martins, M.S. El-Zein (Eds.), Springer Singapore, Singapore, 2020: pp. 67–78. https://doi.org/10.1007/978-981-15-2957-3_5.

[30] K. Treutler, V. Wesling, The Current State of Research of Wire Arc Additive Manufacturing (WAAM): A Review, Appl. Sci. 11 (2021) 8619.

[31] V. Laghi, M. Palermo, G. Gasparini, T. Trombetti, Computational design and manufacturing of a half-scaled 3D-printed stainless steel diagrid column, Addit. Manuf. 36 (2020). https://doi.org/10.1016/j.addma.2020.101505.

[32] H. Kloft, M. Empelmann, N. Hack, E. Herrmann, D. Lowke, Reinforcement strategies for 3D-concrete-printing , Civ. Eng. Des. 2 (2020) 131–139. https://doi.org/10.1002/cend.202000022.

[33] V. Mechtcherine, R. Buswell, H. Kloft, F.P. Bos, N. Hack, R. Wolfs, J. Sanjayan, B.

Nematollahi, E. Ivaniuk, T. Neef, Integrating reinforcement in digital fabrication with concrete: A review and classification framework, Cem. Concr. Compos. 119 (2021) 103964. https://doi.org/10.1016/j.cemconcomp.2021.103964.

[34] J. Müller, M. Grabowski, C. Müller, J. Hensel, J. Unglaub, K. Thiele, H. Kloft, K. Dilger, Design and Parameter Identification of Wire and Arc Additively Manufactured (WAAM) Steel Bars for Use in Construction, Metals (Basel). 9 (2019) 725. https://doi.org/10.3390/met9070725.

[35] V.-A. Silvestru, I. Ariza, J. Vienne, L. Michel, A.M. Aguilar Sanchez, U. Angst, R. Rust, F. Gramazio, M. Kohler, A. Taras, Performance under tensile loading of point-by-point wire and arc additively manufactured steel bars for structural components, Mater. Des. 205 (2021) 109740. https://doi.org/10.1016/j.matdes.2021.109740.

[36] Z. Yu, Z. Pan, D. Ding, J. Polden, F. He, L. Yuan, H. Li, A practical fabrication strategy for wire arc additive manufacturing of metallic parts with wire structures, Int. J. Adv. Manuf. Technol. (2021). https://doi.org/10.1007/s00170-021-07375-x.

[37] V. Laghi, M. Palermo, G. Gasparini, V.A. Girelli, T. Trombetti, Experimental results for structural design of Wire-and-Arc Additive Manufactured stainless steel members, J. Constr. Steel Res. 167 (2020). https://doi.org/10.1016/j.jcsr.2019.105858.

[38] V. Laghi, M. Palermo, L. Tonelli, G. Gasparini, L. Ceschini, T. Trombetti, Tensile properties and microstructural features of 304L austenitic stainless steel produced by wire-and-arc additive manufacturing, Int. J. Adv. Manuf. Technol. (2020) 3693–3705. https://doi.org/10.1007/s00170-019-04868-8.

[39] V. Laghi, M. Palermo, G. Gasparini, M. Veljkovic, T. Trombetti, Assessment of design mechanical parameters and partial safety factors for Wire-and-Arc Additive Manufactured stainless steel, Eng. Struct. 225 (2020). https://doi.org/10.1016/j.engstruct.2020.111314.

[40] V. Laghi, L. Tonelli, M. Palermo, M. Bruggi, R. Sola, L. Ceschini, T. Trombetti, Experimentally-validated orthotropic elastic model for Wire-and-Arc Additively Manufactured stainless steel, Addit. Manuf. 42 (2021) 101999. https://doi.org/10.1016/j.addma.2021.101999.

[41] L. Tonelli, V. Laghi, M. Palermo, T. Trombetti, L. Ceschini, AA5083 (Al–Mg) plates produced by wire-and-arc additive manufacturing: effect of specimen orientation on microstructure and tensile properties, Prog. Addit. Manuf. (2021). https://doi.org/10.1007/s40964-021-00189-z.

[42] L. Tonelli, R. Sola, V. Laghi, M. Palermo, T. Trombetti, L. Ceschini, P.L. Ceschini, P.T.

Trombetti, P. Tomaso Trombetti, Influence of Inter-layer Forced Air Cooling on Microstructure and Mechanical Properties of Wire Arc Additively Manufactured 304L Austenitic Stainless Steel, (n.d.). https://doi.org/10.1002/srin.202100175.

[43] C.-H. Jeon, J.-B. Lee, S. Lon, C.-S. Shim, Equivalent material model of corroded prestressing steel strand, J. Mater. Res. Technol. 8 (2019) 2450–2460.

[44] C.-H. Jeon, C.D. Nguyen, C.-S. Shim, Assessment of mechanical properties of corroded prestressing strands, Appl. Sci. 10 (2020) 4055.

[45] J. Chi-Ho, L. Jae-Bin, S. Chang-Su, Tensile Test of Corroded Strand and Maintenance of Corroded Prestressed Concrete Girders, Int. J. Urban Civ. Eng. 11 (2017) 1384–1388.

[46] M. Morgese, F. Ansari, M. Domaneschi, G.P. Cimellaro, Post-collapse analysis of Morandi's Polcevera viaduct in Genoa Italy, J. Civ. Struct. Heal. Monit. 10 (2020) 69–85.

[47] G.M. Calvi, M. Moratti, G.J. O'Reilly, N. Scattarreggia, R. Monteiro, D. Malomo, P.M. Calvi, R. Pinho, Once upon a time in Italy: The tale of the Morandi Bridge, Struct. Eng. Int. 29 (2019) 198–217.

[48] I. Finozzi, A. Saetta, H. Budelmann, Structural response of reinforcing bars affected by pitting corrosion: experimental evaluation, Constr. Build. Mater. 192 (2018) 478–488.

[49] W. Ramberg, W.R. Osgood, Description of stress-strain curves by three parameters, (1943).

[50] O. Kammouh, S. Silvestri, M. Palermo, G.P. Cimellaro, Performance-based seismic design of multistory frame structures equipped with crescent-shaped brace, Struct. Control Heal. Monit. 25 (2018) 1–17. https://doi.org/10.1002/stc.2079.

[51] MX3D Webpage, (n.d.). www.mx3d.com.

[52] Oerlikon, (n.d.). https://www.oerlikon.com/en/.

[53] ASTM E3-11 Standard Guide for Preparation of Metallographic Specimens, ASTM Int. (2011). https://doi.org/10.1520/E0003-11.2.

[54] M. Steels, Metallography and Microstructures of Stainless steels Maraging steels, ASM Handb. V9. 9 (2004) 1–27. https://doi.org/10.1361/asmhba0003767.

[55] D.W. Hetzner, Etching stainless steels for delta ferrite, Adv. Mater. Process. 165 (2007) 33–34.

[56] Artec 3D webpage, (n.d.). https://www.artec3d.com.

[57] Metallic materials — Tensile testing — Part 1: Method of test at room temperature Matériaux métalliques — Essai de traction — Partie 1: Méthode d'essai à température ambiante COPYRIGHT PROTECTED DOCUMENT, Iso 6892-1. (2009). http://files.instrument.com.cn/FilesCenter/20090913/200991371610112081.pdf.

[58] European Committee for Standardization (CEN), EN 1993 1-4: Eurocode 3 - Design of steel structures, part 1-4: General rules, supplementary rules for stainless steel, (2015).

[59] ASTM A276-16, Standard Specification for Stainless Steel Bars and Shapes, ASTM Int. (2016) 1–8. https://doi.org/10.1520/A0276.

[60] S. Kou, Post-solidification phase transformations, in: Weld. Metall., 2003. https://doi.org/10.1002/0471434027.ch9.

[61] A. Basak, S. Das, Epitaxy and Microstructure Evolution in Metal Additive Manufacturing, Annu. Rev. Mater. Res. 46 (2016) 125–149. https://doi.org/10.1146/annurev-matsci-070115-031728.

[62] O.K. Tokovoi, D. V. Shaburov, Nonmetallic phase in austenitic stainless steel, Steel Transl. 44 (2014) 875–878. https://doi.org/10.3103/S0967091214120183.

[63] Y. Wang, W. Yang, L. Zhang, Effect of Cooling Rate on Oxide Inclusions During Solidification of 304 Stainless Steel, Steel Res. Int. 90 (2019) 1–10. https://doi.org/10.1002/srin.201900027.

[64] T. Hauser, R.T. Reisch, P.P. Breese, Y. Nalam, K.S. Joshi, K. Bela, T. Kamps, J. Volpp, A.F.H. Kaplan, Oxidation in wire arc additive manufacturing of aluminium alloys, Addit. Manuf. 41 (2021) 101958. https://doi.org/10.1016/J.ADDMA.2021.101958.

[65] A. Caballero, J. Ding, Y. Bandari, S. Williams, Oxidation of Ti-6Al-4V during wire and arc additive manufacture, 3D Print. Addit. Manuf. 6 (2019) 91–98.

[66] L. Wang, J. Xue, Q. Wang, Correlation between arc mode, microstructure, and mechanical properties during wire arc additive manufacturing of 316L stainless steel, Mater. Sci. Eng. A. 751 (2019) 183–190. https://doi.org/10.1016/j.msea.2019.02.078.

[67] P. Kyvelou, H. Slack, D.D. Mountanou, M.A. Wadee, T. Ben Britton, C. Buchanan, L. Gardner, Mechanical and microstructural testing of wire and arc additively manufactured sheet material, Mater. Des. (2020) 108675. https://doi.org/10.1016/J.MATDES.2020.108675.

[68] A.L.V. Da Costa E Silva, The effects of non-metallic inclusions on properties relevant to the performance of steel in structural and mechanical applications, J. Mater. Res. Technol. 8 (2019) 2408–2422. https://doi.org/10.1016/J.JMRT.2019.01.009.